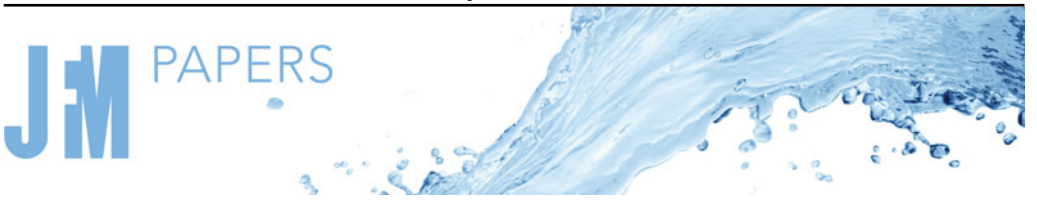
J. Fluid Mech. (2025), *vol.* 1023, A23, doi:10.1017/jfm.2025.10769



Prediction of long-time single-mode Rayleigh–Taylor bubble evolution: a rotational flow model

Changwen Liu[1,2], **Hongzhi Wu-Wang**[2], **Yousheng Zhang**[1,3,4] and **Zuoli Xiao**[1,2,5]

[1]HEDPS, Center for Applied Physics and Technology, School of Mechanics and Engineering Science, Peking University, Beijing 100871, PR China

[2]State Key Laboratory for Turbulence and Complex Systems, School of Mechanics and Engineering Science, Peking University, Beijing 100871, PR China

[3]Institute of Applied Physics and Computational Mathematics, Beijing 100094, PR China

[4]National Key Laboratory of Computational Physics, Beijing 100088, PR China

[5]Nanchang Innovation Institute, Peking University, Nanchang 330008, PR China

Corresponding authors: Yousheng Zhang, qwwzys@163.com; Zuoli Xiao, z.xiao@pku.edu.cn

(Received 4 May 2024; revised 7 September 2025; accepted 29 September 2025)

The nonlinear growth of perturbations in hydrodynamic interfacial instabilities can be of particular importance in both scientific research (e.g. supernova explosion) and engineering applications (e.g. inertial confinement fusion). One of the most significant issues in these instabilities is the long-time nonlinear bubble evolution of a single-mode Rayleigh–Taylor instability (RTI), which remains as an unsolved and challenging problem since Taylor's seminal work more than seven decades ago. Introduced in this paper is an analytical model for the long-time evolution of bubble velocity, curvature and vorticity, which is established by considering the vorticity accumulation around the bubble in a bilaterally rotational flow system under the classical planar potential-flow theory framework. The proposed theoretical model incorporates not only the classical linear, nonlinear and quasi-steady stages, but the late re-acceleration stage. Meanwhile, the new model can capture the phenomenon of secondary velocity saturation following the stage of bubble re-acceleration. The good agreement between the present model and numerical simulations for all density ratios and dimensions confirms that the accumulation in vorticity tends to break the early stage buoyancy-drag equilibrium mechanism and leads to the establishment of a new equilibrium in the late-stage RTI.

Key words: nonlinear instability, fingering instability

© The Author(s), 2025. Published by Cambridge University Press.

https://doi.org/10.1017/jfm.2025.10769 Published online by Cambridge University Press

1. Introduction

The initially perturbed interface separating two fluids with different densities is usually unstable when driven by an acceleration g pointing from aheavy to a light fluid, which is known as the Rayleigh–Taylor instability (RTI) (Rayleigh 1883; Taylor 1950). With the development of such hydrodynamic instability, light and heavy fluids penetrate into each other, resulting in the formation of bubble- and spike-like finger structures (Zhou 2017*a*,*b*). Understanding these phenomena and their underlying mechanisms can be of particular interest in scientific research (e.g. supernova explosion) (Burrows 2000; Isobe *et al.* 2005; Cabot & Cook 2006; Uchiyama *et al.* 2007) and plays important roles in engineering applications (e.g. inertial confinement fusion (ICF)) (Clery 2015; Betti & Hurricane 2016; Casey *et al.* 2017; Ding *et al.* 2017; Matsuo *et al.* 2021; Sabet *et al.* 2021; Ni, Zeng & Zhang 2023; Xie, Xiao & Zhang 2024; Zhang, Le & Tian 2024; Zhou, Sadler & Hurricane 2024). Via modelling analysis, the monograph by Chandrasekhar (1961) summarised several physical effects on the RTI, including surface tension, bulk viscosity, magnetic field, etc. For general reviews of research advances on the RTI, readers are referred to the articles by Sharp (1984), Brouillette (2002), Zhou (2017*a*,*b*), Zhou *et al.* (2019, 2021), ChangWen, ZuoLi & YouSheng (2024) and the book by Zhou (2024). An important issue of the classical RTI is how the finger structures grow in the long-term interfacial evolution due to geometric disturbances. The motivation for interest in the RTI with geometric perturbation at the interface originates from the fact that there might exist interfacial perturbations caused by manufacture (or processing) imperfection (or defect) in the engineering applications, such as the target capsule in the ICF experiments. Due to the complexity of the RTI problem with multi-mode perturbations, this paper focuses on the theoretical modelling of a single-mode planar RTI problem, which is expected to be extended to more complex scenarios such as RTI with multi-mode perturbations, variable acceleration and convergent geometries. There have been several sets of experimental (Jacobs & Catton 1988; Luo, Wang & Si 2013; Luo *et al.* 2018; Liu *et al.* 2018; Liang *et al.* 2019; Lherm *et al.* 2022) and numerical data (Ristorcelli & Clark 2004; Ramaprabhu, Dimonte & Andrews 2005; Li *et al.* 2021; Yan *et al.* 2022) for the evolution of interfacial perturbation growth rate since Taylor's pioneering work in 1950, and yet there is still a lack of theoretical models to analytically predict the long-term evolution of such single-mode fingers.

Previous numerical simulations (Ramaprabhu *et al.* 2012; Wei & Livescu 2012) confirm that the interface evolution of a single-mode RTI usually undergoes the linear stage, nonlinear stage, quasi-steady (QS) stage, re-acceleration (RA) stage and finally enters into the chaotic development (CD) stage (see figure 1). To realise the theoretical prediction of these RTI evolution stages, the classical theory on hydrodynamic instability given by Rayleigh (1883) and its modern development by Taylor (1950) has been continuously extended to form several milestone-like theories, including the potential-flow model (Layzer 1955), the Padé approximation approach (Zhang & Sohn 1997), vortex and vortex sheet models (Jacobs & Sheeley 1996; Matsuoka, Nishihara & Fukuda 2003), the group theory method (Abarzhi 2008), etc. Initially proposed to study the motion of vacuum bubbles with small initial perturbations, Layzer's potential-flow model (LPM) has been extensively employed in studying single-mode fingering instabilities (Hecht, Alon & Shvarts 1994; Alon *et al.* 1995; Zhang & Sohn 1996; Mikaelian 1998, 2003; Zhang 1998; Goncharov 2002; Abarzhi, Glimm & Lin 2003; Sohn 2003; Zhang & Guo 2016; Zhang, Deng & Guo 2018; Guo & Zhang 2020; Zhang & Guo 2022; Liu *et al.* 2023*a*,*b*). This approach considers a system of conservation laws governing the dynamics of an unstable fluid boundary and expands these laws in the vicinity of a regular point at the bubble tip. Thus, the nonlinear boundary value problem for the Euler equations is reduced to a system of ordinary differential equations (ODEs). While Layzer's solution provides a local description of the temporal

https://doi.org/10.1017/jfm.2025.10769 Published online by Cambridge University Press

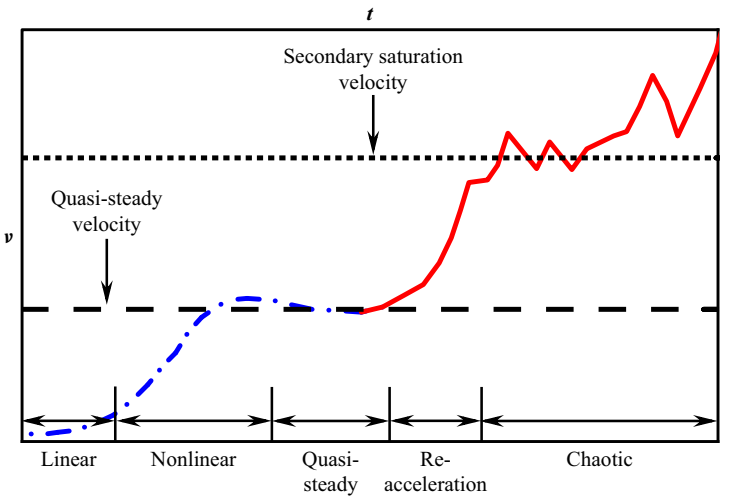


Figure 1. Schematic of different development stages of the RTI based on the numerical result from Wei & Livescu (2012), Ramaprabhu *et al.* (2012) and the sketch map from Zhang & Guo (2016). The blue dash-dotted line represents the classical single-mode RTI stages. The red solid line characterises the later stages without an *a prior* analytical model. The horizontal black dashed line and black dotted line denote the asymptotic values of quasi-steady velocity and secondary saturation velocity, respectively.

evolution of the flow near the bubble tip, it incorporates the dynamics of the entire domain through asymptotic expansion. However, Layzer's approach has notable limitations. It does not take into account the interplay of different modes and the development of singularities in the nonlinear free boundary problem. Although the velocity and curvature of the bubble approach steady values, the acceleration of the spike leads to an infinite curvature of the spike. This divergence property implies that it is challenging to describe the system accurately with a finite number of terms in the expansion. Alternative methods have been established to address these limitations. In recent theoretical advancements, the group theory framework (Abarzhi 2008; Williams & Abarzhi 2021; Abarzhi *et al.* 2023; Chan *et al.* 2023) proves to be able to overcome many of the inherent deficiencies of the LPM. Group theory-based models offer a more robust solution to address these challenges. Nevertheless, the present study aims to provide an objective analysis of the RTI, focusing on the intrinsic physical processes. Therefore, as a well-established model that has been widely utilised by researchers over the past decades, the LPM is selected as the foundation on which the present theoretical model is built. Specifically, the LPM was extended by Hecht *et al.* (1994) to investigate vacuum bubbles in the Richtmyer–Meshkov instability (RMI) . Mikaelian (1998) and Zhang (1998) were among the first to give the evolution of a bubble and spike, respectively, in a fluid-vacuum configuration. Goncharov (2002) generalised the LPM to an arbitrary density ratio, but failed to describe the spike (Mikaelian 2008). Recently, Zhang & Guo (2016), Guo & Zhang (2020) and Zhang & Guo (2022) developed a universal theory for the evolution of fingers (both bubble and spike) with an arbitrary density ratio, which was further employed to solve the RTI problem in a cylindrical geometry (Zhao *et al.* 2020). More recently, Liu *et al.* (2023*b*) introduced a dual-source model within the LPM framework to accurately predict interfacial fingers at all density ratios in both two-dimensional (2-D) and three-dimensional (3-D) cases.

Most of these theoretical models can offer an exact solution to early stage finger evolution, and obtain an asymptotic constant velocity in the QS stage. In the nonlinear stage, the growth rate increases nonlinearly due to the gravity and shape variation of

https://doi.org/10.1017/jfm.2025.10769 Published online by Cambridge University Press

the interface. In the QS stage, however, the growth rate tends to be constant due to the balance between buoyancy and drag forces on both sides of the interface, resulting in a self-similar evolution of the finger structure. Both stages are extremely important and have received extensive attention. Nevertheless, it is noteworthy that all the above theories focus on the development of an instability up to the QS stage, where the vorticity effect can be ignored. After entering the RA stage, the numerical results demonstrate that the vorticity effect dominates the flow field between the bubble and spike, which affects the bubble dynamics and induces new growth of the interface. In light of these observations, Betti & Sanz (2006), Yan *et al.* (2016) introduced a vorticity effect into the LPM for the theoretical study of an ablative RTI, which was subsequently extended to a classical RTI by Ramaprabhu *et al.* (2012) and Bian *et al.* (2020). Incorporating the vorticity effect into the framework of the LPM facilitates a theoretical description of the RTI evolution after the QS stage. Such a modelling strategy can also help shed light on the fact that the RA stage is indeed prompted by the deposition of vorticity near the vertex. However, it should be mentioned that the vorticity is assumed to exist only on the light-fluid side during ablation in this method, which conflicts with actual physics in a classical RTI, especially when the densities of two fluids are close to each other and the vorticities on both sides are comparable with one another. Besides, it is an *a priori* model for bubble evolution, which depends on vorticity evolution data from numerical simulations. Therefore, there still lacks an analytical model to realise an *a posterior* prediction of bubble evolution from the early linear stage to the late RA stage, which motivates the present study.

This paper is intended to develop a new theoretical model to address the long-standing problem for prediction of the RTI bubble evolution within the classical planar LPM framework. The present model is established qualitatively by considering the vorticity accumulation around the bubble, which can mimic the real flow pattern, and is further formulated quantitatively under the constraint of interfacial pressure continuity. The derived equations can simultaneously predict the evolutions of bubble growth rate, spatial curvature and neighbouring vorticity ranging from the classical linear, nonlinear and QS stages to the late RA stage. In addition, the newly developed theoretical model can identify a transient phenomenon known as secondary velocity saturation (SVS) in the bubble evolution of the RTI after the RA stage, as illustrated in figure 1. This phenomenon is also effectively interpreted within the framework of this newly constructed model. All aforementioned results exhibit favourable agreement with numerical data across all density ratios in both 2-D and 3-D cases. The new model represents the first attempt to unveil the nonlinear equilibrium mechanism among bubble growth rate, spatial curvature and neighbouring vorticity, and offer a comprehensive explanation for the origin of the RA stage and SVS phenomenon in later RTI dynamics.

The remaining paper is structured as follows. First, theoretical analysis and derivations are given in § 2. Then, the theoretical model is validated for RTI flows in the linear stage, nonlinear stage, QS stage and RA stage in § 3. Finally, conclusions and discussions are made in § 5. For completeness, the detailed formulations for the present theoretical model are provided in Appendix A.

2. Theoretical analysis and formulations

2.1. *The derivation of classic LPM*

For the purpose of clarity in thesubsequent discussion, the basic idea of the LPM is first introduced for the 2-D case. Specifically, two incompressible inviscid fluids are considered in a vertically infinite channel with the left and right boundaries satisfying the

https://doi.org/10.1017/jfm.2025.10769 Published online by Cambridge University Press

no-penetration condition. The initial material interface is characterised by a single-mode sinusoidal perturbation. The LPM for the RTI problem can be described by the following governing equations (Goncharov 2002; Betti & Sanz 2006):

$$\nabla \cdot \boldsymbol{v}_i = 0, \tag{2.1}$$

$$\partial_t \eta + \boldsymbol{v}_i \cdot \nabla \eta - \boldsymbol{v}_i \cdot \boldsymbol{e}_z = 0 \quad \text{at } z = \eta, \tag{2.2}$$

$$\rho_i (\partial_t \boldsymbol{v}_i + \boldsymbol{v}_i \cdot \nabla \boldsymbol{v}_i + g\boldsymbol{e}_z) = -\nabla p_i, \tag{2.3}$$

$$p_1 = p_2 \quad \text{at } z = \eta. \tag{2.4}$$

Here, x and z are the coordinates perpendicular and parallel to the acceleration g, and $\boldsymbol{e}_x$ and $\boldsymbol{e}_z$ are the unit vectors along the x and z directions, respectively. The subscripts $i = 1, 2$ denote heavy and light fluids, respectively. The velocity vector $\boldsymbol{v}_i$ is related to its potential function φ_i by $\boldsymbol{v}_i \equiv \nabla\varphi_i$ (Pimentel-Garcia 2023), and p_i and ρ_i represent the corresponding pressure and density, respectively. The interface between the two fluids is located at $z = \eta(x, t)$. According to the LPM, the bubble is approximated as a parabola of the form $\eta(x, t) = z_0(t) + \xi(t)x^2$, where $z_0(t)$ and $\xi(t)$ are the vertical position and curvature of the bubble, respectively. For the ideal incompressible fluids consider in this study, both the kinematic and dynamic conditions are imposed at the interface of the two fluids. The kinematic condition at the interface ensures that fluid particles cannot penetrate the interface, i.e. the normal velocities of the fluid particles on both sides of the interface are equal to each other. This can be represented by the kinematic equation of the interface (2.2), which is derived by establishing the material derivative $\mathrm{D}F(x, z, t)/\mathrm{D}t = 0$ with $F(x, z, t) = z - \eta(x, t) = 0$ since the two fluids share the same material interface. Applying (2.2) to both fluids can readily yield a zero jump in normal velocity across the interface (denoted by $[\boldsymbol{v} \cdot \boldsymbol{n}] = 0$, with $\boldsymbol{n}$ being the unit normal vector at the interface). For the dynamic condition at the interface, the continuity of pressure is ensured across the interface (denoted by $[p] = 0$ or (2.4)). In addition, the fluid is stationary and undisturbed at the far-field boundaries along the flow direction (z), i.e. $\boldsymbol{v}_i(z \to \pm\infty) = \nabla\varphi_i(z \to \pm\infty) = 0$. In the spanwise direction (x), only the velocity component along the flow direction is allowed at the boundary since the evolution of a complete single-mode interface is considered in the present study. Therefore, the spanwise velocity boundary condition can be described as a no-penetration condition, i.e. $v_{i,x}(x = \pm(\lambda/2)) = \partial_x\varphi_i(x = \pm(\lambda/2)) = 0$. Thus, given a reasonable initial spatial distribution of the flow field, the bubble evolution can be obtained from the interface kinematic condition (2.2) and the momentum equation(2.3) under the pressure continuity condition (2.4) at the interface.

2.2. *Analysis of the classic LPM framework*

Within the framework of the classical LPM, the sinusoidal potential function is employed to approximate the flow dynamics near the fingertip and in its immediate vicinity. While this approach approximately satisfies the dynamic condition of constant surface pressure, it assumes a time-invariant fingertip shape when predicting the growth rate. This assumption, however, conflicts with numerical simulations reported by Sohn (2004) and Ramaprabhu & Dimonte (2005), leading to unphysical predictions of the growth rate (Krechetnikov 2009). Furthermore, the theoretical validity of potential functions without harmonics or singularities remains questionable as pointed out by Kull (1983). Additionally, the gravitational acceleration predicted by the sinusoidal potential-flow model exhibits a rapid increase below the fingertip, with the trend intensified for

https://doi.org/10.1017/jfm.2025.10769 Published online by Cambridge University Press

larger initial amplitudes (Kull 1986). This result highlights a significant discrepancy considering the fact that the predicted acceleration is non-uniform across the flow field, whereas a conservative force such as gravitational acceleration should remain uniform. Consequently, the LPM struggles to capture the global flow characteristics such as the intense fluid motion localised near the interface and the negligible motion far from the interface.

Despite these limitations, the classical LPM performs reasonably well in describing the growth rates, which depend only weakly on acceleration uniformity. However, it fails to accurately predict the curvature of the fingertip, a more sensitive parameter that varies with the Atwood number A. According to Chan *et al.* (2023), the LPM predicts a less curved bubble tip but a more curved spike compared with numerical simulations. Although some experiments and numerical simulations appear to agree with LPM predictions, such agreement might be superficial as these investigations usually feature low spatial and temporal resolutions, limited observation time scales (approximately one decade) and a restricted set of diagnostic parameters.

This paper aims to provide an objective analysis of the RTI during the RA and SVS stages, emphasising the intrinsic physics of these processes. To this end, a dual-source model is proposed by introducing a dual-source velocity potential function in a uniform incoming flow. This approach accurately captures the streamline distribution and significantly improves the predictive performance of the potential-flow model, especially under low-density ratio conditions, as demonstrated by Liu *et al.* (2023*a*). However, it should be mentioned that our approach has its limitations, which include the lack of rigorous justification for dual-source hypothesis, the approximate nature of the solution along a 'line' of vertices and the primary focus on local rather than global flow characteristics. Nevertheless, as a robust theoretical framework that has been widely employed by researchers over the past decades, the LPM provides a valuable tool for the present study.

2.3. *The LPM for the later stages*

For convenience in the following discussion, we show in figures 2(*a*) and 2(*b*) the flow fields at two extremely important and distinctive stages, i.e. the QS and RA stages, of RTI evolution with an Atwood number of $A = 0.3$, which are obtained in anumerical simulation using an in-house code CFD^2 (Zhang *et al.* 2020). The Atwood number is defined as the relative density ratio in the form $A \equiv (\rho_1 - \rho_2)/(\rho_1 + \rho_2) \in [0, 1]$, which is frequently used for a unified description of the RTI flows (Zhang & Guo 2016). Detailed introductions of the numerical methods and input parameters are provided in § 3.

In most of previous investigations, the focus is placed on the bubble evolution up to the QS stage. The physical image at the QS stage (see figure 2*a*) shows that the vorticity generated at the interface remains localised in its neighbourhood, which implies that the vorticity-induced velocity at the bubble front is negligible (Layzer 1955). For this reason, the classical LPMs consider an irrotational flow system to further simplify the governing equations (2.1)–(2.4) by introducing the velocity potential function φ. However, as shown in figure 2(*b*), the vorticity has already accumulated around the bubble when the RTI evolution enters the RA stage. At this point, the frontal vorticity-induced velocity cannot be ignored, which breaks the standard equilibrium (Betti & Sanz 2006) between buoyancy and drag forces, and the bubble velocity no longer follows the prediction of the classical LPM. As discussed above, there is no available analytical theory that can properly predict the bubble evolution beyond the QS stage to date. To this end, a novel theory is proposed in this paper by considering a bilaterally rotational flow system.

https://doi.org/10.1017/jfm.2025.10769 Published online by Cambridge University Press

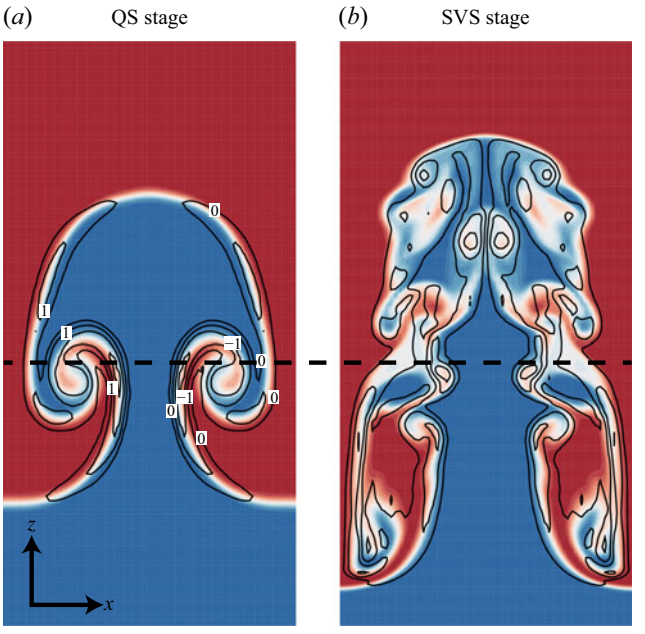


Figure 2. Vorticity distributions of the RTI flow field at the QS stage (*a*) and SVS stage (*b*) obtained from the present numerical simulation ($A = 0.3$), which are overlaid on contours of mass fraction. The finger is generated by the penetration of heavy fluid (red) into light fluid (blue). The black solid lines visualise the contours of vorticity. The black dashed line indicates the initial interface.

The velocity vector in the RTI can be decomposed into two parts according to the Helmholtz theorem:

$$\boldsymbol{v}_i = \nabla\varphi_i + \nabla \times \psi_i, \quad \nabla \cdot \psi_i = 0. \tag{2.5}$$

Here φ_i is the scalar potential and ψ_i is the vector potential. The vorticity field is then given by

$$\boldsymbol{\omega_i} = \nabla \times \boldsymbol{v}_i = \nabla \times (\nabla \times \psi_i). \tag{2.6}$$

For incompressible flow, (2.6) is further simplified to

$$\boldsymbol{\omega_i} = -\nabla^2\psi_i. \tag{2.7}$$

For a given vorticity distribution, one can solve for the vector potential from (2.7) with prescribed boundary conditions. Alternatively, one can obtain the vorticity distribution readily from (2.7) for a constructed vector potential. For the RTI, the vorticity effect can be ignored before the RA stage, and the velocity field can automatically degenerate into the solution of a classical LPM. After the QS stage, however, the modulation of vorticity-induced velocity becomes prominent with the increase in vorticity accumulation effect. Moreover, although the bubble undergoes a complex nonlinear evolution, the pressure at the interface always satisfies the continuity condition to avoid breakup of the interface, which essentially imposes an important constraint for the flow around the interface. Based on these considerations, the present modelling approach comprises two key steps. A coherent velocity field is first constructed by incorporating features of both potential-flow and rotational flow regimes on both sides of the interface, and then the relationship between the velocity fields on either side is determined through the pressure continuity condition at the interface.

https://doi.org/10.1017/jfm.2025.10769 Published online by Cambridge University Press

A qualitative analysis of figure 2 can be instructive to properly construct the model of the flow field. As is clearly seen, the development of potential velocity (in the bulk) and vortex structures is indeed confined to the vicinity of the interface, and their intensities are localised around the bubble vertex. This is because the dynamics of the RTI in the early stage are inherently concentrated at the interface and its vicinity, with their effects rapidly diminishing at locations far way from the interface. In addition, the vorticities are symmetrically distributed around the vertex and cancel out each other at the bubble vertex. In this sense, the derivation of the present model should be based on these physical pictures.

For a rotational flow system, it is assumed that the velocity field is given by the superposition of a potential flow and a prescribed rotational flow. Formally, the potential flow can be described by the general velocity potential function that satisfies the Laplace equation $\nabla^2\varphi_i = 0$ with the corresponding boundary conditions as aforementioned . In the LPM, the 2-D and 3D potential functions φ_i are written as (Liu *et al.* 2023*b*)

$$\varphi_i = Q_i(t)\sum_{n=0}^{\infty}\frac{\cos[(2n+1)kx]}{(2n+1)}\mathrm{e}^{(-1)^i(2n+1)k(z-z_0+a_i(t))} \quad \text{(2D)}, \tag{2.8}$$

and

$$\varphi_i = Q_i(t)\sum_{n=0}^{\infty}\frac{\cos\left[(2n+1)k_{3D}^{x}x\right]\cos\left[(2n+1)k_{3D}^{y}y\right]}{(2n+1)}\mathrm{e}^{(-1)^i(2n+1)k_{3D}(z-z_0+a_i(t))} \quad \text{(3D)}, \tag{2.9}$$

respectively, where $k \equiv 2\pi/\lambda$ is the wavenumber. However, it poses big challenge in practical computations if one retains the complete form of the Fourier series. The series truncation in LPMs has been a long-standing challenge in modelling nonlinear RTI dynamics. It is noted that Abarzhi (1995, 1996*a*,*b*) is among the first to systematically analyse the truncation effects based on the group theory approach, demonstrating that the optimal truncation order depends on the interface symmetry and higher-order harmonics must satisfy conservation laws. It is also shown that the truncation error scales as $\mathcal{O}(n^{-3/2})$ for n retained modes. These findings help fundamentally shape the subsequent developments in potential-flow models, including the present work. While different mathematical tools are employed in the present LPM-based approach, the use of a physical principle for mode selection can be of particular importance based on energy conservation within the group theory framework. Besides, the series truncation in LPMs has been further addressed via group-theoretic principles (Abarzhi 1998, 1999). We retain terms up to $n = 2$ in the Fourier series for φ_i and ω_i, ensuring a third-order spatial accuracy. For $n = 2$, the relative error in v_{RT} is reduced to less than 3 %, validating the convergence of the truncated system. Considering that the LPM method essentially provides an approximate solution along a 'line' of vertices, Goncharov (2002) demonstrates that higher-order series expansions can improve model accuracy without significantly altering the predictive trends. Specifically, retaining only the first two terms in each series can provide a solution with up to 95 % accuracy. This indicates that including only the first two orders of the Fourier series is sufficient to capture the main features of large-scale coherent motion in the RTI. Therefore, to simplify the calculation, we take the first term $n = 0$ for φ_1 and the first two terms $n = 0$, 1 for φ_2 to describe the complex flow structures inside the bubble. As for the rotational flow part, the vorticity is related to velocity by $\nabla \times \boldsymbol{v}_i = \boldsymbol{\omega}_i$. Here ω_i is the vorticities for species i (the corresponding flow patterns can be seen in figures 2*a* and 2*b*), which vanishes at the peaks and troughs of the interface and is strongest roughly at a middle position between them, but lightly skewed to the spike side.

https://doi.org/10.1017/jfm.2025.10769 Published online by Cambridge University Press

Therefore, it is assumed that the interfacial vorticity distribution should be approximated as a sinusoidal function, with its extreme points located near the interfacial centres and its zero point located at the finger front of bubbles and spikes. According to the numerical results (Glimm, Li & Lin 2002; Sohn 2011), the vorticity is stronger at the spike side than at the bubble side. In this study, the sinusoidal function also considers the variation of vorticity in the z direction to make vorticity generation more reasonable near the spike side. In addition, it is noted in figure 2 that the evolution of vorticity is concentrated near the interface and decays rapidly to zero far away from the interface. This behaviour is consistent with that of the velocity potential function field. It indicates that the dynamic characteristics of the RTI are primarily localised at the interface, with intense fluid motion occurring in its vicinity and successively weak motions farther away from the interface. Based on this phenomenological analysis, it is conjectured that the vorticity takes the simple form $\boldsymbol{\omega_i} = -\omega_i(t)\sin(kx)\exp[(-1)^i k(z-z_0)]\boldsymbol{e}_y$.

The vorticity ansatz $\omega_i = -\omega_i(t)\sin(kx)e^{(-1)^i k(z-z_0)}$ in our model ensures that vorticity is confined to the interface region and decays exponentially with distance from the interface. The characteristic decay length $L_d \sim k^{-1}$ is determined solely by the initial perturbation wavenumber k, consistent with rigorous theoretical analyses of an inviscid RTI (Abarzhi 2008; Williams & Abarzhi 2022). This aligns with the group-theoretic framework, where the interfacial vorticity structures are localised within a distance proportional to the initial wavelength $\lambda = 2\pi/k$, independent of viscous effects.

The exponential decay profile ($\sim \mathrm{e}^{-k|z|}$) of the proposed vorticity aligns with the asymptotic analytical solutions from Zhou *et al.* (2019), who derived interfacial vorticity confinement in an inviscid RTI. This also confirms that the vorticity decay length scale is governed solely by the initial conditions, not viscosity.

However, due to the complexity in solving the vorticity-induced velocity and the fact that the proposed model focuses on the flow in the vicinity of the bubble vertex, the expressions for the velocity field are only given at the vertex ($z = \eta$). By combing both flow regimes, the velocity at the bubble front ($z = \eta$) can be written as

$$\boldsymbol{v}_i = \nabla\varphi_i + \frac{3\omega_i(t)\cos(kx)}{2k}\boldsymbol{e}_z. \tag{2.10}$$

Given that the planar RTI evolves only along the flow direction, the 3-D model can be extended from the 2-D model by employing a centrally symmetric approach (Liu *et al.* 2023*a*,*b*). Therefore, for 3-D cases such as the RTI flow in a square box (Yan *et al.* 2016; Guo & Zhang 2020), the symmetry of this specific configuration leads to a potential function φ_i in a series form $\varphi_i = Q_i(t)\sum_{n=0}^{\infty}\{\cos[(2n+1)k_{3D}^x]\cos[(2n+1)k_{3D}^y]\exp[(-1)^i(2n+1)k(z-z_0+a_i(t))]/(2n+1)\}$, where, $k_{3D}^x = k_{3D}^y = k/\sqrt{2}$ denotes the wave numbers in the two horizontal directions. Meanwhile, the corresponding vorticity can be written as $\boldsymbol{\omega_i} = -\omega_i(t)exp[(-1)^i k/\sqrt{2}(z-z_0)]\ \sin(k_{3D}^x)\sin(k_{3D}^y)(\boldsymbol{e}_x + \boldsymbol{e}_y)$. Other settings are the same as those in the 2-D case. Consequently, the velocities at the bubble front in the 3-D case read

$$\boldsymbol{v}_i = \nabla\varphi_i + \frac{9\omega_i(t)\cos(k_{3D})}{2k_{3D}}\boldsymbol{e}_z. \tag{2.11}$$

Considering the continuity of interfacial pressure, one can derive the constraint relation governing the velocity fields on both sides of the interface. As mentioned previously, the velocity field can be decomposed into two distinct components, i.e. the velocity induced by potential forces and that induced by vorticity. While the velocity component induced by constant gravitational acceleration g has been extensively studied within the classical LPM, our focus is placed on analysis of the constraint imposed on the vorticity-induced

https://doi.org/10.1017/jfm.2025.10769 Published online by Cambridge University Press

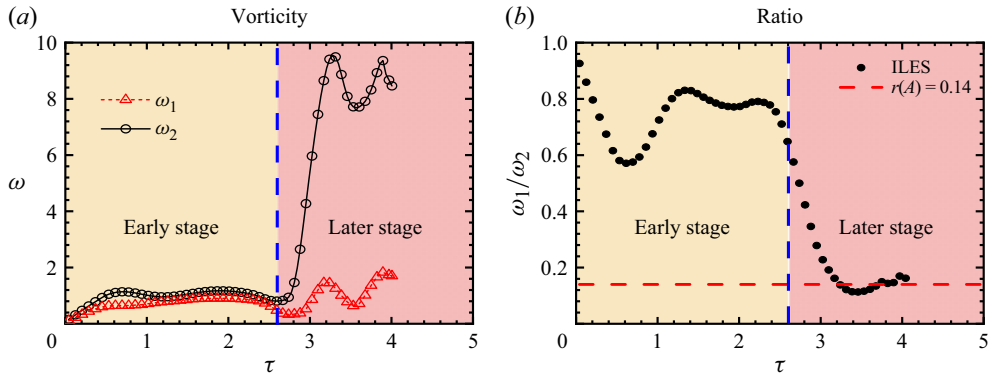


Figure 3. Evolutions of (*a*) the bubble vorticities on both the light- (ω_2) and heavy-fluid (ω_1) sides and (*b*) the vorticity ratio around the bubble tip obtained in present numerical simulations of a 2-D RTI at $A = 0.3$ using CFD[2].

velocity component. The vorticities are calculated around the bubble tip on both the light- and heavy-fluid sides, which are shown in figure 3(*a*) with respect to time. It is observed that the vorticity (ω_2) for the light fluid is much larger in the late stage than in the early stage. For the heavy fluid, however, the vorticity (ω_1) remains relatively small throughout the entire range of time. In fact, it is seen that ω_1 and ω_2 are comparable with each other during the early stage of the RTI evolution. In other words, the influence of vorticity around the bubble tip can be negligible in the early stage of the RTI development. The ratio $r(A) = \omega_1/\omega_2$ is derived up to third order by solving the expanded pressure continuity condition. The revised expression

$$r(A) = 0.2(1 - A) + 0.05(1 - A)^2 + \mathcal{O}((1 - A)^3) \tag{2.12}$$

improves agreement with numerical data (figure 3*b*, dashed curve). Stability analysis confirms that $r(A)$ remains invariant under perturbations to the initial vorticity distribution. As one can see, the vorticities on both sides of the bubble tip are close to each other in the early stage (on the left-hand side of the vertical dashed line), especially in the QS stage where there exists a local plateau with a value of about 0.8. After the QS stage, however, the curve drops drastically and tends to converge to a constant value of 0.16 during the SVS stage. Although the vorticity ratio is time dependent from the early to late stages, a constant assumption during the SVS stage is reasonable for a given Atwood number. In light of the above numerical analysis, it is conjectured that the ratio of bubble-tip vorticites on the light- and heavy-fluid sides can be written as

$$r(A) = \frac{\omega_1(t)}{\omega_2(t)}, \tag{2.13}$$

which varies with A. Here, we assume that the ratio $r(A)$ is a constant value throughout the entire stage, which hardly influences the prediction accuracy of the model in the early stage RTI evolution because the vorticity effect around the bubble tip is negligible during these stages. According to relation (2.13), the vorticity on the light-fluid side can be expressed in the form $\omega_2 = r(A)\omega_1(t)$.

In summary, there are three unknowns to be determined in the present model for prediction of the RTI interface evolution, i.e. z_0, ξ and ω_1, provided that the vorticity ratio is given *a priori* or empirically. Following the LPM, the present model only solves the RTI problem in the neighbourhood of the fingertip instead of the whole interface. Thus, the

https://doi.org/10.1017/jfm.2025.10769 Published online by Cambridge University Press

series expansions in the x direction (as well as the potential functions and the interfacial vorticity functions) are valid in the neighbourhood of the bubble vertex. As a result, the auxiliary parameters Q_1, Q_2, a_1 and a_2 can be solved by substituting expansions of φ_1 and φ_2 into (2.2) and expanding the resultant equations to the order of x^2. The amplitude of potential functions and interfacial vorticity functions can be obtained from (2.3) of the bubble vertex. Therefore, in order to close the current model, one needs to further integrate (2.3) and expand through orders of x^2 and x^4 in (2.4), respectively, to yield the following ODEs:

$$\dot{\xi} = F(k, r, \xi, v, \omega_1), \tag{2.14}$$

$$S_1 g + S_2 v^2 + S_3 \dot{v} + S_4 v\omega_1 + S_5 \omega_1^2 + S_6 \dot{\omega}_1 = 0, \tag{2.15}$$

$$T_2 v^2 + T_3 \dot{v} + T_4 v\omega_1 + T_5 \omega_1^2 + T_6 \dot{\omega}_1 = 0. \tag{2.16}$$

Here, $v = \mathrm{d}z_0/\mathrm{d}t$ is the bubble velocity; $F(k, r, \xi, v, \omega_1)$ can be obtained from (2.2) in both 2-D and 3-D cases; $S_p(A, k, r, \xi, v, \omega_1)$ and $T_p(A, k, r, \xi, v, \omega_1)$ $(p = 1, \cdot s, 6)$ are coefficients of the x^2 and x^4 terms in (2.3) and (2.4). The detailed expressions of these coefficients are obtained with the aid of Mathematica 11.2 (Wolfram Research, Inc., 2017) and provided in Appendix A for reference. It should be pointed out that the LPM focuses on the time evolution of the bubble and physical quantities in its neighbourhood. Hence, the interfacial vorticity in the LPM corresponds to the neighbouring vorticity around the bubble, which reflects the accumulation of vorticity therein.

By solving the ODEs (2.14)–(2.16), it is found that there exist two fixed points with $\dot{v} = 0, \dot{\xi} = 0$ and $\dot{\omega}_1 = 0$. Accordingly, the bubble velocity, curvature and the neighbouring vorticity converge to constant values. For the first fixed point, the neighbouring vorticity around the bubble approaches zero (i.e. $\omega_1 \sim 0$) and can be ignored. This corresponds to the classical asymptotic behaviour of the RTI in the QS stage. As for the second fixed point, the neighbouring vorticity converges to a non-zero constant, which is significantly larger than that for the first fixed point. The second plateau corresponds to a new asymptotic behaviour that is rarely reported in literature.

Linear stability analysis of the ODEs (2.14)–(2.16) reveals that the QS and SVS fixed points are asymptotically stable. The Jacobian matrix $\mathcal{J}$ at these points has eigenvalues with negative real parts (i.e. $\mathrm{Re}(\lambda_1, \lambda_2, \lambda_3) = (-0.12, -0.08, -0.05)$) for $A = 0.3$. This ensures that small perturbations decay exponentially, corroborating the numerical observations and confirming an asymptotic stability.

To explore the newly identified characteristic behaviour, comparisons are made between existing numerical simulations, which successfully capture the RA stage of a single-mode RTI (Glimm *et al.* 2002; Ramaprabhu *et al.* 2012; Wei & Livescu 2012; Bian *et al.* 2020). The collective findings show that, at high Reynolds numbers, the bubble growth rate momentarily reaches a stationary state during the transition from the end of the RA stage to the early CD stage, but is characterised by fluctuations around a constant value (as depicted in figure 2*b* of Wei & Livescu 2012). After that, the growth rate continues to increase linearly with time during the CD stage. However, as the Reynolds number decreases, various stages of the single-mode RTI are observed to gradually disappear due to the viscous effects except in the nonlinear stage. Given the good consistency between the properties of a single-mode RTI by solving the Euler equation system and Navier–Stokes equation system at high Reynolds numbers, it is inferred that this new velocity saturation phenomenon corresponds to a transient stage from the end of the RA stage to the early CD stage, as illustrated in figure 1. During this stage, vortex pairs reach the mixing layers at the tip of the bubble, thereby limiting the increase in induced velocity.

https://doi.org/10.1017/jfm.2025.10769 Published online by Cambridge University Press

Reference	Dimension	Code	Atwood numbers A	Reynolds number Re_p
Zhang *et al.* (2020)	2D	CFD^2	0.3,0.7	∞
Zhang *et al.* (2020)	3D	CFD^2	0.3,0.7	∞
Bian *et al.* (2020)	2D	DiNuSUR	0.04,0.8	20000
Bian *et al.* (2020)	3D	DiNuSUR	0.04,0.25,0.6	1000, 8000
Ramaprabhu *et al.* (2012)	3D	RTI-3D	0.15,0.25,0.7	∞

Table 1. A list of numerical simulations to validate the theoretical model.

Meanwhile, the continuous augmentation of vortical motions near the centreline, where the shear velocity is the largest, quickly leads to complex vortex interactions, influencing the velocity induced by vorticity and causing significant fluctuations. Therefore, this phenomenon is termed the 'secondary velocity saturation' . To the best of the authors' knowledge, this marks the first theoretical realisation of this particular stage.

It should be mentioned that the present model does not consider the effects of viscosity and surface tension, rendering it applicable only to situations at high Reynolds numbers. If the method introduced by Sohn (2009) is employed to take into account the effects of viscosity and surface tension, the model can be further utilised to analyse the mechanism of the successive disappearance of various stages at low-Reynolds-number conditions.

Based on the physical implications of these two fixed points, it is further inferred that bubbles achieve the velocity saturation due to the standard equilibrium between buoyancy and drag forces at the QS stage. However, with the increase of neighbouring vorticity, the vorticity-induced velocity breaks this standard equilibrium and triggers the re-acceleration of bubbles. Furthermore, the combined effects of gravity and vorticity establish a new equilibrium at the interface, resulting in a novel SVS phenomenon in the early chaotic stage. Therefore, by simultaneously considering the potential force-induced component from potential flow and vorticity-induced component from rotational flow, the coupled system can accurately describe the bubble evolution up to the early chaotic stage of a single-mode RTI.

3. Validation of the theoretical model

Since the present theoretical model is derived from Euler equations, the model is validated through comparison with numerical simulations based on Euler equations (or in the infinite Reynolds number limit) as well as simulations based on Navier–Stokes equations at high Reynolds numbers. Listed in table 1 are all the simulation cases used for validation of the model along with the corresponding dimensions, Atwood numbers and Reynolds numbers $Re_p \equiv \lambda\sqrt{(A/(1+A))g\lambda}/\nu$, where ν is kinematic viscosity. Specifically, comparative discussions are provided for the results of both 2-D and 3-D cases.

At first, in order to validate the new theoretical model, numerical simulations are carried out using an in-house code CFD^2 (code of finite difference for compressible fluid dynamics) based on a finite difference method (Zhang *et al.* 2020). This code has been successfully applied to numerical simulations of flows induced by the RTI and RMI (Zhang *et al.* 2020). Specifically, this code is set to numerically solve the compressible Euler equations along with the mass fraction equation. The convection terms are discretised by using the fifth-order weighted essentially non-oscillating scheme (Jiang & Shu 1996) and solved with the Roe Riemann solver (Roe 1981; Sanders, Morano & Druguet 1998). A third-order total variation diminishing Runge–Kutta method

https://doi.org/10.1017/jfm.2025.10769 Published online by Cambridge University Press

(Gottlieb & Shu 1998) is adopted for the time integration. The flow field is initialised with a state of hydrostatic equilibrium (i.e. $\boldsymbol{u_i} = 0$) and thermal equilibrium ($T = 1$) (see, e.g. Reckinger, Livescu & Vasilyev 2011).

The input parameters and initial values are set to $g = 1$, $k = 1$, $\xi^0 = -0.15$ and $v^0 = 0$. As mentioned above, the vorticity ratio $r(A)$ needs to be prescribed with respect to A for implementation of the present model. Pre-calculations for the cases of $A = 0.3$ and $A = 0.7$ based on CFD^2 suggest that $r(A)$ should take a linear form, i.e. $r(A) = 0.2(1 - A)$ for the 2-D case and $r(A) = 0.1(1 - A)$ for the 3-D case, which also apply to the extreme cases of $A = 1$ (fluid–solid configuration) and $A = 0$ (equal density). A leading motivation for employing LPMs in this study is that the values of bubble/spike velocities given by the LPMs show quantitative agreement with numerical simulations (Goncharov 2002; Zhang & Guo 2016). It should be mentioned that these characteristic velocity values are first derived rigorously within the group theory framework (Williams & Abarzhi 2021, 2022; Chan *et al.* 2023), which provides the universal scaling $v \sim \sqrt{Ag\lambda}$ for asymptotic velocities, the exact velocity prefactors for all Atwood numbers, and the dimensional dependence (2-D versus 3-D) of growth rates. While the group theory offers fundamental insights, the LPMs remain valuable for their mathematical tractability in analysing vorticity effects, as demonstrated in the present research work. The consistency between both approaches confirms the robustness of these velocity predictions.

To numerically demonstrate that vorticity decay far from the interface is associated only with the initial length scale, not kinematic viscosity, numerical simulations based on the in-house code CFD^2 are analysed within a Reynolds number range of $Re_p = 10^3$–10^5. Across all cases, the vorticity magnitude decays exponentially with a fixed length scale $L_d \approx 0.16\lambda$ (calculated from k^{-1}), consistent with the inviscid limit. This confirms that the decay mechanism is dominated only by the initial wavelength λ, not the viscous dissipation. These results align with the results reported by Williams & Abarzhi (2021), where viscosity mainly affects secondary instabilities, but hardly alters the primary vorticity distribution. The comprehensive numerical study by Bian *et al.* (2020) also suggests that the vorticity decay length L_d remains governed by λ across a wide range of Re_p (10^3–10^5). Their results show that while viscosity modifies small-scale fluctuations, the primary confinement scale $L_d \sim k^{-1}$ persists independently of Re_p, directly supporting the assumptions of the present model.

Shown in figure 4(*a–f*) are evolutions of the 2-D bubble velocity, spatial curvature and neighbouring vorticity at $A = 0.3$ and $A = 0.7$, covering all mentioned stages. It should be stressed that the vorticity given by this model is close to zero up to the QS stage. Therefore, a disturbance is supplemented according to the numerical results to make the solution converge to the SVS stage. Moreover, the cutoff series of φ_i lead to a smaller curvature prediction (Goncharov 2002), but the effect of curvature is reflected in its change rate (Liu *et al.* 2023*a*,*b*). Therefore, the asymptotic curvature value (ξ^{SVS}) at the SVS stage is employed to rescale the model and simulation results for comparison purposes. Likewise, the corresponding results under the same conditions for 3-D cases are depicted in figures 5(*a*) and 5(*b*). It should be mentioned that only the results for velocity are provided here due to the difficulty of measuring 3-D spatial curvature and neighbouring vorticity.

As can be seen in figure 4(*a–d*), the bubble velocity and spatial curvature of the classical single-mode RTI predicted by the present theoretical model almost collapse onto the data from numerical simulations in the linear stage, nonlinear stage and QS stage. By contrast, there exists a significant difference in the neighbouring vorticity between the theoretical model and numerical simulations (see figures 4*e* and 4*f*). The neighbouring vorticity given

https://doi.org/10.1017/jfm.2025.10769 Published online by Cambridge University Press

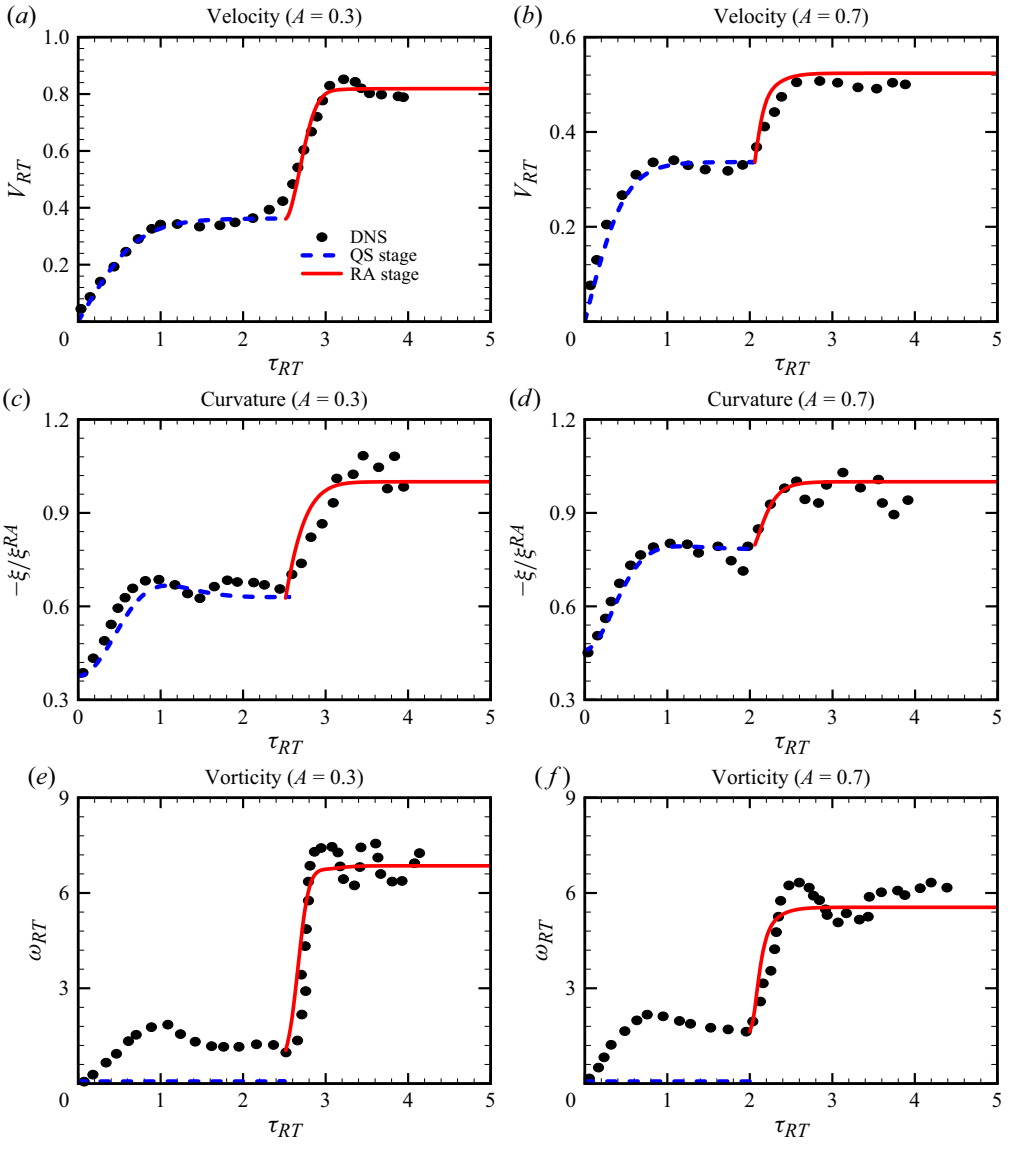


Figure 4. Evolutions of the 2-D RTI bubble velocity (*a*,*b*), spatial curvature (*c*,*d*) and neighbouring vorticity (*e*,*f*) predicted by the present theoretical model (blue dashed lines and red solid lines). The results from numerical simulations (black solid circles) using CFD[2] are also plotted for comparison.

by the former always approaches zero, while that calculated in the latter evolves in time with non-zero values. It can also be seen from numerical data (figures 4*e* and 4*f*) that ω_{RT} in the early stage is negligible if the value at the QS stage is compared with that at the SVS stage. Taking into account the vorticity distributions as observed in figure 2(*a*), one can draw a conclusion that the neighbouring vorticity ω_{RT} in the early stage is approximately negligible. In practice, although the modelled vorticity tends to be zero, it does not affect the performance of this theoretical model in the prediction of the velocity and curvature up to the QS stage. This verifies the consistency between the current model and classical LPM before the RA stage.

https://doi.org/10.1017/jfm.2025.10769 Published online by Cambridge University Press

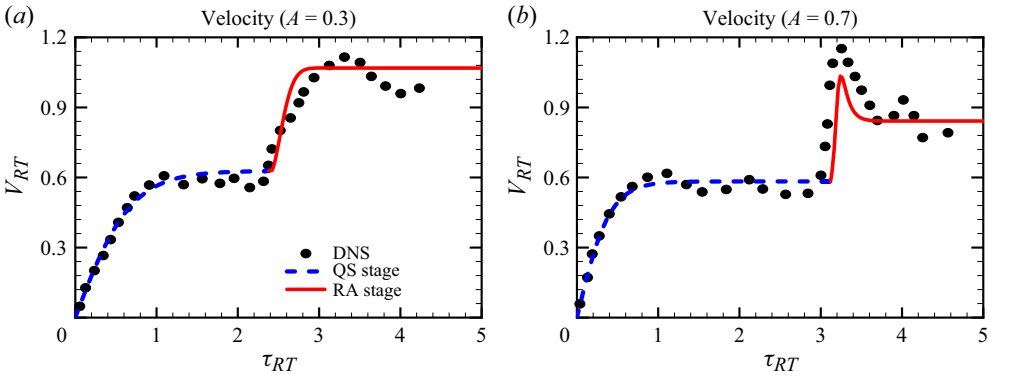


Figure 5. Evolutions of the 3-D RTI bubble velocity at $A = 0.3$ (a) and $A = 0.7$ (b) predicted by the present theoretical model (blue dashed lines and red solid lines). The results from numerical simulations (black solid circles) using CFD[2] are also included for comparison.

For the single-mode RTI bubble evolution after the QS stage, the theoretical results can be obtained by imposing a disturbance on the neighbouring vorticity according to the numerical results. Comparisons in figure 4(a–d) imply that the bubble velocity, curvature and neighbouring vorticity predicted by the model are all consistent with the results from numerical simulations in the RA and SVS stages. These results also show that the new theoretical model successfully captures the physical mechanism behind the re-acceleration of bubbles after the QS stage. When the vorticity effect cannot be ignored and begins to dominate the flow field, the bubble front will be affected by the vorticity-induced velocity and accelerate again. With the secondary acceleration of the bubble, the amount of light fluid penetrating into the heavy-fluid side increases accordingly, leading to an increase in drag. Finally, the bubble velocity in the rotational flow system will enter the SVS stage.

It is also noted that there exist fluctuations in bubble velocity calculated from numerical simulations (see figures 4a,b and 5a,b), which are more intense in the SVS stage than in the QS stage. Correspondingly, the curvature and neighbouring vorticity also exhibit similar phenomena as seen in figure 4(c–f). Here, we try to provide some preliminary explanations. In the early stage with negligible vorticity ($\omega_{RT} \sim 0$), the flow field is subjected to constant gravitational acceleration, resulting in more stable changes in interface and curvature. However, the effect of neighbouring vorticity on the bubble front changes with the breakdown and generation of vortices. Therefore, when the vorticity effect begins to dominate the flow field, the bubble velocity, curvature and neighbouring vorticity quickly converge to the SVS stage, but oscillate around the asymptotic values. In other words, the theoretical model provides a definite asymptotic value, while the numerical simulation gives an oscillating result around the corresponding asymptotic value.

To further evaluate the performance of the new model, the modelled results are compared with those from recent numerical simulations of a single-mode RTI (Bian *et al.* 2020) at high Reynolds numbers $Re_p = 1000$, 8000 and 20 000. These high-resolution fully compressible simulations are carried out using a code named DiNuSUR to study the late-time behaviour of bubbles at both low and high Atwood numbers. Shown in figures 6(a,b) and 7(a–c) are evolutions of the bubble velocity for the 2-D RTI and 3-D RTI, respectively, at different Reynolds numbers. The non-dimensionlisation of velocity is the same as before, but the time here is normalised as $\tau = \sqrt{Ag/\lambda}t$.

https://doi.org/10.1017/jfm.2025.10769 Published online by Cambridge University Press

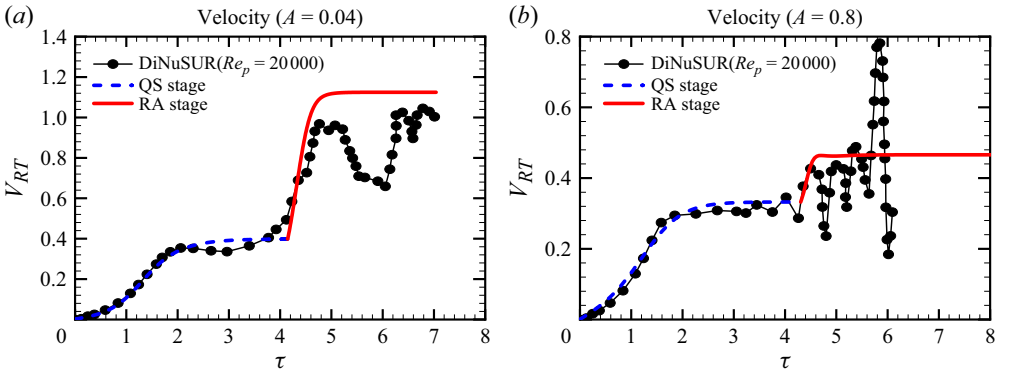


Figure 6. Evolutions of the 2-D RTI bubble velocity at $A = 0.04$ (*a*) and $A = 0.8$ (*b*) predicted by the present theoretical model (blue dashed lines and red solid lines). The results from numerical simulations (black solid circles) using DiNuSUR (Bian *et al.* 2020) at $Re_p = 20\,000$ are also included for comparison.

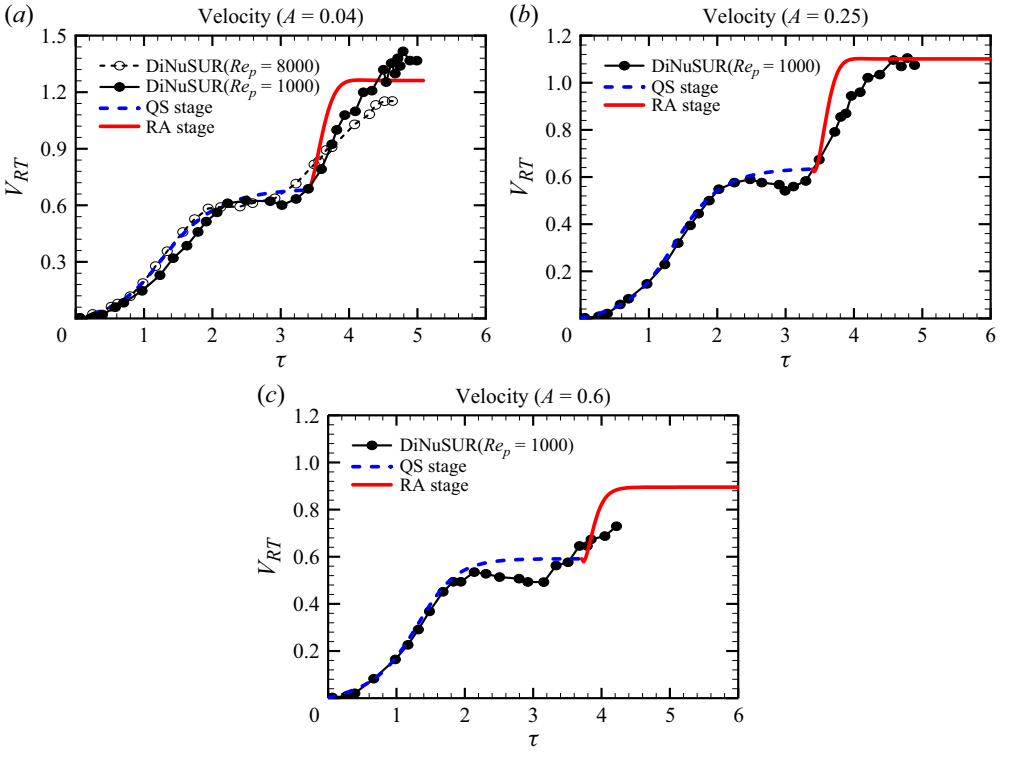


Figure 7. Evolutions of the 3-D RTI bubble velocity at $A = 0.04$ (*a*), $A = 0.25$ (*b*) and $A = 0.6$ (*c*) predicted by the present theoretical model (blue dashed lines and red solid lines). The results from DiNuSUR numerical simulations (Bian *et al.* 2020) at $Re_p = 8000$ (black solid circles) and $Re_p = 1000$ (black open circles) are also included for comparison.

As can be seen in figure 6(*a*,*b*), the results given by the present model are in good consistency with those from the numerical simulations at Reynolds number $Re_p = 20\,000$. It is noted that the new model overpredicts the value of the SVS by about 10 % at the SVS stage in comparison with numerical simulations, which might be attributed to

https://doi.org/10.1017/jfm.2025.10769 Published online by Cambridge University Press

the overestimated vorticity due to the absence of viscosity in the modelling procedure. In addition, strong oscillations of the bubble velocity appear during the SVS phase, whereas no similar phenomena are observed in the QS stage. This is consistent with the results calculated by our in-house code CFD^2 that solves Euler equations with numerical or artificial viscosity. Since viscosity directly affects the generation and dissipation of vorticity, these comparisons indicate that the re-acceleration at the late stage is indeed dominated by vorticity. As a result, the effect of viscosity on vorticity causes more severe fluctuations in velocity at the SVS stage.

Similar results can be seen in figure 7(*a–c*) for 3-D cases with Reynolds numbers $Re_p = 1000$ and $Re_p = 8000$. It turns out that the present model performs as well as expected at low Reynolds numbers if one takes the numerical simulation results as references. In fact, as depicted in figure 7(*c*), the velocity from the numerical simulation still keeps increasing at the final moment, which indicates that the 3-D RTI simulation has not fully entered the SVS stage and converged to a SVS value. This showsthat a reliable theoretical model can be of particular importance in predicting the late-stage behaviour of the RTI in the sense of saving the huge computational cost needed for 3-D numerical simulations.

The above discussion shows that the present theoretical model, which is constructed in the framework of Euler equations, can achieve very good performance in comparison with numerical simulations at high Reynolds numbers. According to the research by Wei & Livescu (2012), however, an obvious deviation in the evolution of the growth rate can be observed when the Reynolds number decreases, and only when the Reynolds number is sufficiently large (i.e. when the Reynolds number exceeds a critical value) will the multiple evolution stages of growth rate occur including the RA and subsequent stages. In other words, all existing models in the potential-flow framework (including the present one) are not suitable for the prediction of the RTI at relatively low Reynolds numbers. This is due to the fact that the Reynolds number essentially reflects the strength of viscosity with other characteristic quantities remaining unchanged. As mentioned in Banerjee *et al.* (2011), Ramaprabhu *et al.* (2012), the viscous effect introduced within the framework of potential-flow theory is primarily reflected in the momentum equation

$$\rho_i(\partial_t \boldsymbol{v}_i + \boldsymbol{v}_i \cdot \nabla \boldsymbol{v}_i + g\boldsymbol{e}_z) = -\nabla p_i + \mu_i \nabla^2 \boldsymbol{v}_i. \tag{3.1}$$

Therefore, the factors dominating the interface evolution of a single-mode RTI increase to four terms when the viscous effect is taken into account, i.e. inertia-induced velocity, deformation-induced velocity, vorticity-induced velocity and viscous drag. This implies that the viscous resistance effect in the RTI interface evolution increases with the decrease of Reynolds number, leading to a competition and balance among these four coupled mechanisms within the flow field. For discussions on related issues based on the potential-flow theoretical model, readers are referred to Banerjee *et al.* (2011) and Ramaprabhu *et al.* (2012). The effects of various physical processes on the growth rate, especially the effect of Reynolds number (or viscous dissipation), are a crucial issue and are open for subsequent studies.

As aforementioned, both the velocity and vorticity at the bubble vertex will be successively suppressed with the increase in Atwood number as demonstrated in figures 5(*e*) and 5(*f*), which show that there exists an obvious discrepancy between the bubble vertex vorticities for $A = 0.3$ and $A = 0.7$ at the SVS stage. This is consistent with the observations by Betti & Sanz (2006) and Yan *et al.* (2016) that the development of vorticity is significantly inhibited on the high-density fluid side in high-Atwood-number scenarios. The containment of the bubble vertex neighbouring vorticity weakens the acceleration during the RA stage of the interface evolution. Although a detailed

https://doi.org/10.1017/jfm.2025.10769 Published online by Cambridge University Press

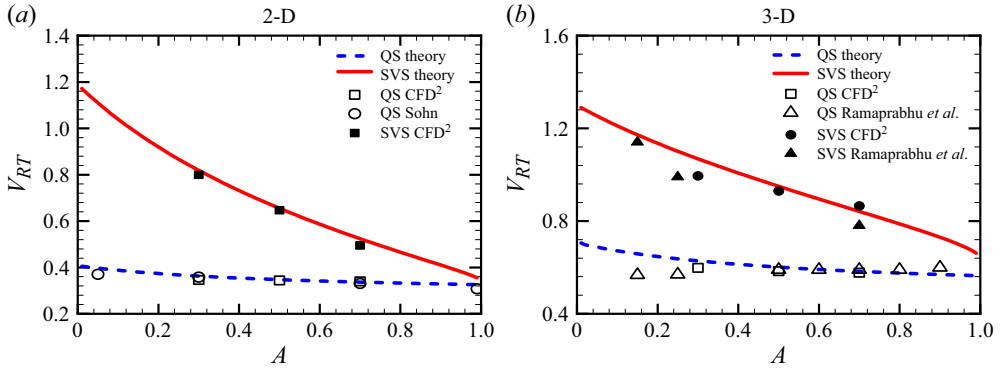


Figure 8. The RTI bubble velocity with respect to the Atwood number given by the new theory at QS (blue dashed lines) and SVS (red solid lines) stages for (*a*) 2-D and (*b*) 3-D cases. The present numerical results (CFD^2) at the QS stage (black solid squares) and SVS stage (black open squares) are included for comparison. The 2-D numerical results at the QS stage (black open circles) reported by Sohn (2004) and the 3-D numerical results at the QS stage (black open triangles) and SVS stage (black solid triangles) reported by Ramaprabhu *et al.* (2012) are also provided as supplement to the present numerical data.

theoretical analysis can be conducted for high-Atwood-number cases, rare existing numerical simulations can provide predictions for the RA and subsequent stages of a single-mode RTI at very high Atwood numbers (e.g. when $A > 0.9$). This is due to the difficulty encountered in numerical simulations to ensure the symmetry property of a single-mode RTI bubble evolution at high Atwood numbers. Meanwhile, the large pressure gradient across the interface in high-density ratio scenarios leads to slow computational speed and high computational cost.

To the best of our knowledge, the present theoretical model is among the first to be able to simultaneously achieve such satisfactory predictions for v_{RT}, ξ_{RT} and ω_{RT} in all mentioned stages. This new model clearly reveals that the bubble growth rate is strongly affected by neighbouring vorticity after the QS stage, which is one of its advantages compared with previous theories and numerical simulations. This also indicates that with the vorticity accumulation around the bubble front, the vorticity-induced velocity breaks the standard balance between buoyancy and drag forces in potential flow, which is dominated only by gravitation. Instead, the effects of gravity and vorticity seek to bring the interface into a new balance, which causes the re-acceleration of bubbles. Therefore, it is believed that the consideration of a bilaterally rotational flow system is the key to success of this new theory.

The asymptotic behaviour is extremely important for a RTI flow (Clery 2015; Betti & Hurricane 2016; Casey *et al.* 2017; Ding *et al.* 2017; Matsuo *et al.* 2021; Sabet *et al.* 2021). As can be seen from figures 4 and 5, the bubble velocity, spatial curvature and neighbouring vorticity are nearly independent of time (i.e. $\dot{v} \approx 0$, $\dot{\xi} \approx 0$ and $\dot{\omega}_1(t) \approx 0$) in both QS and SVS stages. In such situations, (2.14)–(2.16) can be reduced to the following form:

$$\dot{\xi} = F(k, r, \xi, v, \omega_1), \tag{3.2}$$

$$S_1 g + S_2 v^2 + S_4 v\omega_1 + S_5 \omega_1^2 = 0, \tag{3.3}$$

$$T_2 v^2 + T_4 v\omega_1 + T_5 \omega_1^2 = 0. \tag{3.4}$$

Thus, the corresponding asymptotic values can be algebraically solved from (3.2)–(3.4). Figures 8(*a*) and 8(*b*) compare the asymptotic bubble velocities at the QS and SVS stages

https://doi.org/10.1017/jfm.2025.10769 Published online by Cambridge University Press

within a wide range of Atwood numbers A between the current theory and numerical simulations for 2-D and 3-D cases, respectively. A functional form of v^{SVS} can be obtained by applying the least-square method to the present data, which is formally similar to Liu *et al.*'s formulation (Liu *et al.* 2023*b*) and reads

$$v^{SVS} \approx \sqrt{f(A)\frac{2A}{1+A}\frac{g}{k}}, \tag{3.5}$$

where $f(A) = f_{2D}(A) = (4-3A)/(1+2A)$ and $f(A) = f_{3D}(A) = (15-8A)/(3+2A)$ are for 2-D and 3-D cases, respectively. It is shown in figures 8(*a*) and 8(*b*) that the SVS velocities of bubbles predicted by the present theory are in very good agreement with those given by the present numerical simulations based on CFD^2 (Zhang *et al.* 2020) and the 3-D numerical simulation conducted by Ramaprabhu *et al.* (2012). In addition, the asymptotic growth rate of the bubble decreases with the increase of density ratio at the SVS stage. This implies that the effect of vorticity on the growth rate in the SVS stage tends to be suppressed with the increase of density ratio as mentioned above. In addition, the RA and subsequent phases can nearly disappear as the Atwood number A approaches 1 in consistence with figures 8(*a*) and 8(*b*), which shows that the velocity at the SVS stage decreases monotonically and tends to approach that at the QS stages as A goes to 1 for both 2-D and 3-D cases. This observation further supports the physical mechanism that the occurrence of RA and subsequent stages in a single-mode RTI is primarily driven by the interfacial vorticity, reinforcing the validity of the present theoretical model.

4. Discussions

This paper is intended to provide an objective analysis of the RTI during the RA and SVS stages, with an emphasis on the intrinsic physics governing these processes. The aim is to elucidate these phenomena by integrating the classical potential-flow model with the effect of vorticity. In our previous research work (Liu *et al.* 2023*b*), it is observed that Zufiria's point-source model (Zufiria 1988) aligns well with the streamlines obtained from numerical simulation. Accordingly, we proposed a dual-source model by introducing a dual-source velocity potential function and superimposing an incoming flow, which accurately captures the streamline distribution within the flow field. Furthermore, by analysing the interfacial vorticity distribution from numerical simulations and recognising that vorticity is concentrated near the interface, an approximate distribution of the vorticity is assumed within the flow field. While viscosity modifies small-scale features (e.g. fluctuations in the SVS stage), it does not alter the fundamental scaling of vorticity decay. The agreement between present model and high-Re_p simulations (e.g. figure 4) supports this conclusion.

The new model improves the classical potential-flow theory by coupling velocity, curvature and vorticity, leading to a set of third-order differential equations. This improvement in modelling strategy upgrades the predictive performance of the potential-flow theoretical model, especially under low-density ratio conditions, as discussed by Liu *et al.* (2023*b*). In addition, these considerations are based on the intention to characterise the motion of interface near the vertex and its vicinity. Although good comparisons are reported between some experimental and numerical results and the LPM solution, such agreement could be questionable. This is because these studies often feature limitations such as low spatial and temporal resolutions, a limited dynamic range of observation time and only a subset of diagnostic parameters. It is also necessary to acknowledge the drawbacks of the present approach within the LPM framework. Furthermore, the dual-source model relies on an assumption about the flow structures,

https://doi.org/10.1017/jfm.2025.10769 Published online by Cambridge University Press

which may not be universally valid. Secondly, the assumptions underpinning the present model may not hold for regions far from the vertex since the LPM provides an approximate solution along a 'line' of vertices. Moreover, the model primarily focuses on the local evolution at interfacial vertices, limiting its ability to capture global characteristics, such as interaction classifications and pattern formations. Finally, the derivation of Layzer-type solutions may involve violations of conservation laws, further complicating the theoretical foundation of the model.

While the LPM method used in this study can provide a basic analysis of certain low-order statistical quantities at the interface vertex, such as growth rate and curvature, its inherent limitations prevent one from a detailed characterisation of RTI evolution. Meanwhile, these limitations may lead to unforeseen issues in analysis of the RTI development during later stages. As a promising alternative, the new approach based on group theory for prediction of a single-mode RTI development (Abarzhi 2008; Williams & Abarzhi 2021; Abarzhi *et al.* 2023; Chan *et al.* 2023) addresses many shortcomings encountered in the use of the LPM framework. The group-theory approach allows a description of the RTI that aligns with physically observable velocity fields, satisfies zero-velocity boundary conditions and conservations of mass, momentum and energy, and shows quantitative agreement with existing results. Models based on group theory demonstrate superior performance under low-density ratio conditions and higher accuracy under high-density ratio conditions compared with classical potential-flow theory models. Therefore, for the limitations identified in the LPM method, a model based on group theory may provide a more robust solution. Firstly, the group theory-based model inherently avoids mass sources in spatially extended fluid systems, thereby ensuring compliance with boundary conditions and conservation laws. Secondly, the local expansions used in the group-theory model ensure the derivation of asymptotic dynamics of the nonlinear RTI bubble to the leading order in time while accounting for higher-order spatial correlations. The resultant RTI families of local asymptotic solutions are comprehensive, encompassing all possible solutions allowed by the spatial symmetry of the flow. Furthermore, the model construction considers dynamics of the entire field, rather than being confined to a local region. In addition, the group-theory approach highlights the symmetry and order in RTI dynamics, including the emergence of periodic coherent structures at the interface. This group-theory based approach enables a comprehensive study of both local evolutionary properties such as asymptotic behaviour of the bubble front, and global characteristics such as interaction classifications and pattern formation.

Group theory offers a robust framework for investigating a wide range of RTI-related nonlinear problems, accommodating various symmetries for $0 < A \leqslant 1$. It can help establish invariants and scaling laws for coherent motion, identify novel features in the nonlinear evolution of unstable fluid interfaces and introduce new parameters for experiment and numerical simulation diagnostics. While the improved potential-flow theory framework employed in this paper can offer a qualitative and quantitative description of the physical characteristics in the later stages of a single-mode RTI, it is believed that adopting a group theory-based approach would enable a more comprehensive investigation on subsequent stages such as RA and SVS. The incorporation of the aforementioned group theory in the modelling procedure is left for our future research. The objective is to achieve a more accurate description and more detailed analysis of late-stage RTI flows by considering the promising group-theory concept, especially from the perspective of the entire flow field, thereby enhancing our understanding of RTI dynamics.

https://doi.org/10.1017/jfm.2025.10769 Published online by Cambridge University Press

5. Conclusion

In conclusion, a new analytical model is developed for the long-time evolution of the RTI by introducing a bilaterally rotational flow system, which is distinguished from previous scenarios within the LPM framework. The new theory is established qualitatively by combining the gravity force from potential flow and the vorticity accumulation around the bubble, which can mimic the real flow pattern, and is further formulated quantitatively under the constraint of interfacial pressure continuity. It is believed that the newly proposed methodology can simultaneously describe the dynamics of a single-mode RTI flow in both classical stages (including the linear stage, nonlinear stage and QS stage) and the later regimes (RA stage and SVS stage in the early chaotic stage). In the new model, destruction and reconstruction of the equilibrium between buoyancy and the drag force caused by the superposition of potential force-induced velocity and vorticity-induced velocity are taken into account, which may be the major obstacle to development of an accurate theory for the long-time bubble evolution. By introducing the bilaterally rotational flow system into the governing equations, the derived ODE system can simultaneously capture the bubble velocity, spatial curvature and neighbouring vorticity. For the first time, the present theoretical model can successfully predict the long-time RTI bubble evolution from the linear stage all the way down to the SVS stage, which is characterised by early chaotic behaviour. The predicted bubble velocity, spatial curvature and neighbouring vorticity agree well with the numerical simulations at all density ratios in different dimensions, which demonstrates the validity of the present theoretical model. It turns out that the bubble will undergo a secondary acceleration process when the vorticity-induced velocity begins to dominate the flow field, which causes the bubble to leave the classical QS stage and enter the later stages. These phenomena can be well explained using the proposed theoretical model.

We comment that, in the classical RTI stages, the neighbouring vorticity at the bubble front is negligible, and the vorticity-induced velocity can be neglected. Under such circumstances, the initially perturbed interface evolves primarily due to the influence of potential force-induced velocity. As more light fluid penetrates into the heavy-fluid side, the drag on the bubble's surface increases correspondingly. Consequently, the bubble reaches the QS stage due to the standard equilibrium between buoyancy and drag forces. However, the significance of vorticity-induced velocity is gradually pronounced with the accumulation of vorticity around the bubble. This breaks the standard equilibrium, and leads to the acceleration of the bubble in the RA stage. Nevertheless, the RA stage is not indefinitely sustainable. The re-acceleration may usually persist until the vortex pairs reach the mixing layers at the bubble's tip, where the induced velocity cannot increase any more. As a result, a new equilibrium at the interface emerges due to the coupled effect of vorticity and gravity, leading to the occurrence of the SVS phenomenon in the early chaotic stage. Meanwhile, the continuous generation of vortical motions near the centreline, where the shear velocity is most pronounced, causes the intricate vortex interactions, which have an important influence on the velocity induced by vorticity and result in significant fluctuations.

The invariance of vorticity decay length $L_d \approx 0.16\lambda$ across all numerical simulations with varying Re_p confirms that the decay mechanism of vorticity is dominated only by the initial wavelength λ, not the viscous dissipation. This aligns with the results reported by Williams & Abarzhi (2022), Chan *et al.* (2023) where viscosity mainly affects secondary instabilities, but hardly alters the primary vorticity distribution. The agreement of our model with high-Re_p data validates this decay property of vorticity in both 2-D and 3-D cases.

https://doi.org/10.1017/jfm.2025.10769 Published online by Cambridge University Press

Furthermore, the successive generation and breakdown of vortices promote the single-mode RTI into the CD stage characterised by aperiodic behaviour and extreme sensitivity to initial conditions. The mechanism uncovered in this study provides readers with a clearer understanding of the overall development of a single-mode RTI.

The new theoretical model proposed in this paper may provide a new direction for controlling interfacial instabilities. Furthermore, It is anticipated that the new theory should find applicability in better understanding the variable acceleration problems (Dimonte, Ramaprabhu & Andrews 2007; Mikaelian 2009, 2010; Ramaprabhu *et al.* 2016) because the change in acceleration does not alter the velocity saturation properties. However, although the theoretical model and numerical simulations are in good agreement in the early stage, there exist certain errors in the late stage, which may be attributed to two factors. One is the attenuation of vorticity-induced velocity caused by viscous dissipation in numerical simulations. The other is the assumption of sinusoidal vorticity, which does not apply to the late SVS stage of the RTI any more. It is noteworthy that most of the numerical simulations and experiments of a RMI/RTI are concentrated on the dynamics of a gaseous interface, in which the effect of surface tension is usually neglected. In fact, it is indeed reasonable to ignore the surface tension force in the high-pressure and high-temperature environment, such as the implosion in ICF. Therefore, the effect of surface tension is neglected in the present model. It should be pointed out that, given the surface tension coefficient, the surface tension can be readily incorporated into the present framework since the interface curvature evolution has already been taken into consideration in our model. To some extent, the present study sheds light on the mechanisms of long-time bubble evolution for a single-mode RTI. If insight is further taken into the phenomenon of bubble–bubble interaction, it is possible to better understand the resultant turbulent mixing or the evolution of a multi-mode RTI, which is much closer to realistic engineering applications.

Funding. We acknowledge the financial support provided by the National Natural Science Foundation of China (Grant Nos. 92152202, 12222203, 12588301,12532013) and the National Key Laboratory of Computational Physics (Grant No. 6142A05240201).

Declaration of interests. The authors report no conflict of interest.

Appendix.

In this appendix we present the concrete expressions for (2.14)–(2.16). The derivations for the 2-D case are firstly introduced as follows. As mentioned in the paper, the velocities for both upstream and downstream flows and the corresponding potential functions in the 2-D case can be written as

$$\boldsymbol{v}_i = \nabla\varphi_i + \frac{3\omega_i(t)\cos(kx)}{2k}\boldsymbol{e}_z, \tag{A1}$$

$$\varphi_i = Q_i(t)\sum_{n=1}^{\infty}\frac{\cos[(2n+1)kx]e^{(-1)^i(2n+1)k(z-z_0)}}{2n+1}. \tag{A2}$$

Substituting expressions (A1) and (A2) into (2.2), and expanding the resultant equations to the orders of x^2 and x^4, one can solve the coefficient F explicitly and the solution takes the form

$$F(k, r, \xi, v, \omega_1) = -\frac{1}{2}k(k+6\xi)v + 4r\xi\omega_1. \tag{A3}$$

https://doi.org/10.1017/jfm.2025.10769 Published online by Cambridge University Press

After substituting the above expressions into (2.3) and (2.4), one can readily obtain two ODEs through the orders of x^2 and x^4 as follows:

$$S_1 g + S_2 v^2 + S_3 \frac{dv}{dt} + S_4 v\omega_1 + S_5 \omega_1^2 + S_6 \frac{d\omega_1}{dt} = 0, \tag{A4}$$

$$T_2 v^2 + T_3 \frac{dv}{dt} + T_4 v\omega_1 + T_5 \omega_1^2 + T_6 \frac{d\omega_1}{dt} = 0. \tag{A5}$$

Here, $v = dz_0/dt$ is the front velocity; $S_p(A, c, \xi, k, r)$ and $T_p(A, c, \xi, k, r)$ $(p = 1, 2, 3, 4, 5, 6)$ are the coefficients of the x^2 and x^4 expansion terms in (2.3) and (2.4); $T_1 = 0$ is ignored because the term ηg in (2.3) is constrained by $\eta(x, t) = z_0(t) + \xi(t)x^2$, which only contains the x^2 terms; $S_p(A, c, \xi, k, r)$ and $T_p(A, c, \xi, k, r)$ take the following forms:

$$S_1 = A\xi, \tag{A6}$$

$$S_2 = \frac{k^2\big((-3 + 7A)k^2 + 6(-5 + 3A)k\xi + 9A\xi^2\big)}{2(2k - 3\xi)^2}, \tag{A7}$$

$$S_3 = \frac{2k^2 + Ak\xi - 6A\xi^2}{4k - 6\xi}, \tag{A8}$$

$$S_4 = -\frac{1}{4}\left(2kr(1 + A) + \frac{2k(-1 + A)\big(2k^2(3 + r) + 4k(5 + 11r)\xi + 3(1 + 4r)\xi^2\big)}{(2k - 3\xi)^2}\right), \tag{A9}$$

$$S_5 = \frac{1}{4(2k - 3\xi)^2}\Big(4k^2\big(-1 + A + r^2 + Ar^2\big) + 4k\big(-1 + A - 12r + 12Ar - 11r^2 + 5Ar^2\big)\xi + \big(-1 + A - 8r + 8Ar - 7r^2 + 25Ar^2\big)\xi^2\Big), \tag{A10}$$

$$S_6 = \frac{-2k(1 + r + A(-1 + r)) + (-1 + A - r + 7Ar)\xi}{8k - 12\xi}, \tag{A11}$$

$$T_2 = \frac{1}{24(2k - 3\xi)^2}\big(k^2\big((39 - 43A)k^4 + 18k^3\xi(13 - 15A) + 3k^2\xi^2(-420 + 481A) + 36k\xi^3(-10 + 3A) + 108A\xi^4\big)\big), \tag{A12}$$

$$T_3 = \frac{k\big(-2k^3 + 3k^2\xi(-12 + 5A) - 12k\xi^2(-10 + 9A) + 36A\xi^3\big)}{48k - 72\xi}, \tag{A13}$$

$$T_4 = \frac{1}{48}\left(kr(1 + A)(5k^2 - 48\xi^2) + \frac{1}{(2k - 3\xi)^2}\big(k(-1 + A)\big(4k^4(18 + 13r) + 4k^3\xi(211 + 250r) - 15k^2\xi^2(181 + 272r) - 48k\xi^3(31 + 19r) - 144\xi^4(-1 + 2r)\big)\big)\right), \tag{A14}$$

$$T_5 = \frac{1}{12(2k - 3\xi)^2}\big(-4k^4\big(-1 + A + r^2 + Ar^2\big) - 4k^3\xi\big(-19 - 48r - 29r^2 + A\big(19 + 48r + 23r^2\big)\big) + k^2\xi^2\big(-155 - 484r - 329r^2 + A\big(155 + 484r$$

https://doi.org/10.1017/jfm.2025.10769 Published online by Cambridge University Press

$$+407r^2\big)\big)-48k\xi^3\big(3+8r+5r^2+A(-3-8r+r^2)\big)+12\xi^4\big(-1+A+4r$$
$$-4Ar+5r^2+13Ar^2\big)\big), \tag{A15}$$

$$T_6=\frac{1}{48(2k-3\xi)}\big(2k^3(1+r+A(-1+r))+k^2\xi(49(1+r)-A(49+55r))$$
$$+48k\xi^2(-3(1+r)+A(3+5r))-24\xi^3(1+r+A(-1+5r))\big). \tag{A16}$$

Given the initial values, the solutions to the above ODEs can be easily obtained by iteration and integration with time t.

By following a similar procedure, one can obtain the expressions for upstream and downstream velocities and the corresponding potential functions for the 3-D case (2.11) in the following forms:

$$\boldsymbol{v}_i=\nabla\varphi_i+\frac{9\omega_i(t)\cos(k_{3D})}{2k_{3D}}\boldsymbol{e}_z, \tag{A17}$$

$$\varphi_i=Q_i(t)\sum_{n=1}^{\infty}\frac{\cos\left[(2n+1)\frac{kx}{\sqrt{2}}\right]\cos\left[(2n+1)\frac{ky}{\sqrt{2}}\right]e^{(-1)^i(2n+1)k(z-z_0)}}{2n+1}. \tag{A18}$$

Likewise, substituting (A17) and (A18) into (2.2)–(2.4), one can reach two ODEs through the orders of x^2 and x^4, which are exactly the same as (A4) and (A5). Finally, one ends up with the following coefficients:

$$F(k,r,\xi,v,\omega_1)=-\frac{1}{4}k(k+8\xi)v+\big(1+2\sqrt{2}\big)r\xi\omega_1, \tag{A19}$$

$$S_1=A\xi, \tag{A20}$$

$$S_2=\frac{k^2\big((-1+2A)k^2+4(-3+2A)k\xi+4A\xi^2\big)}{8(k-2\xi)^2}, \tag{A21}$$

$$S_3=\frac{k^2+2Ak\xi-8A\xi^2}{4k-8\xi}, \tag{A22}$$

$$S_4=-\frac{1}{32}\big(4\sqrt{2}kr(1+A)+\frac{1}{(k-2\xi)^2}\big(k(-1+A)\big(k^2\big(1+6\sqrt{2}+r+2\sqrt{2}r\big)$$
$$+4\big(1+2\sqrt{2}\big)k\xi(3+7r)+8\xi^2\big(1+r+2\sqrt{2}r\big)\big)\big)\big), \tag{A23}$$

$$S_5=\frac{1}{16(k-2\xi)^2}\big(2k^2\big(-1+A+r^2+Ar^2\big)+2k\xi\big(-(1+r)\big(\sqrt{2}+(13+4\sqrt{2})r\big)$$
$$+A\big(\sqrt{2}+(13+5\sqrt{2})r+(5+4\sqrt{2})r^2\big)\big)+\xi^2\big(A+\big(2+4\sqrt{2}\big)Ar$$
$$+\big(17+4\sqrt{2}\big)Ar^2-(1+r)\big(1+r+4\sqrt{2}r\big)\big)\big), \tag{A24}$$

$$S_6=\frac{-\sqrt{2}k(1+r+A(-1+r))+\big(-1-r+A(1+r+4\sqrt{2}r)\big)\xi}{8k-16\xi}, \tag{A25}$$

$$T_2=\frac{1}{192(k-2\xi)^2}\big(k^2\big((13-11A)k^4-8k^3\xi(-3+4A)+8k^2\xi^2(-138$$
$$+151A)-384Ak\xi^3+384A\xi^4\big)\big), \tag{A26}$$

https://doi.org/10.1017/jfm.2025.10769 Published online by Cambridge University Press

$$T_3 = -\frac{k\left(k^3 - 2k^2\xi(-12+A) + 144k\xi^2(-1+A) - 96A\xi^3\right)}{96(k-2\xi)}, \tag{A27}$$

$$\begin{aligned} T_4 = {} & \frac{1}{768}\left(4kr(1+A)\left(\sqrt{2}k^2 - 36k\xi - 96(2+\sqrt{2})\xi^2\right) + \frac{1}{(k-2\xi)^2}\left(k(-1+A)\right.\right. \\ & \left(k^4\left(13+30\sqrt{2}+13(1+2\sqrt{2})r\right) + 8k^3\xi\left(21+36\sqrt{2}+29(1+2\sqrt{2})r\right)\right. \\ & - 16k^2\xi^2\left(31+237\sqrt{2}+187(1+2\sqrt{2})r\right) + 192k\xi^3\left(-21+1(4+8\sqrt{2})r\right) \\ & \left.\left.\left. - 768\xi^4\left(-3+r+2\sqrt{2}r\right)\right)\right)\right), \end{aligned} \tag{A28}$$

$$\begin{aligned} T_5 = {} & \frac{1}{192(k-2\xi)^2}\left(-4k^4\left(-1+A+r^2+Ar^2\right) + k^3\xi\left(48+28\sqrt{2}+(181+68\sqrt{2})r\right.\right. \\ & + \left(133+64\sqrt{2}\right)r^2 - A\left(48+28\sqrt{2}+\left(181+68\sqrt{2}\right)r+\left(101+40\sqrt{2}\right)r^2\right)\Big) \\ & + 2k^2\xi^2\left(-179-36\sqrt{2}-2\left(311+76\sqrt{2}\right)r-\left(443+164\sqrt{2}\right)r^2+A\left(179+36\sqrt{2}\right.\right. \\ & \left. + 2\left(311+76\sqrt{2}\right)r+\left(619+308\sqrt{2}\right)r^2\right)\Big) - 48k\xi^3\left(2+5\sqrt{2}+9\left(1+2\sqrt{2}\right)r\right. \\ & + \left(7+11\sqrt{2}\right)r^2 + A\left(-2-5\sqrt{2}-9\left(1+2\sqrt{2}\right)r+\left(25+19\sqrt{2}\right)r^2\right)\Big) \\ & \left.\left. + 48\xi^4\left((1+r)\left(-1+(7+12\sqrt{2})r\right)+A\left(1-6\left(1+2\sqrt{2}\right)r+5\left(5+4\sqrt{2}\right)r^2\right)\right)\right), \end{aligned} \tag{A29}$$

$$\begin{aligned} T_6 = {} & \frac{1}{192(k-2\xi)}\left(\sqrt{2}k^3(1+r+A(-1+r)) + k^2\xi\left(\left(13+24\sqrt{2}\right)(1+r) - A\left(13\right.\right.\right. \\ & \left.\left.\left. + 24\sqrt{2}+\left(13+28\sqrt{2}\right)r\right)\right) + 48k\xi^2\left(-3\sqrt{2}(1+r)+3\sqrt{2}A+\left(4+5\sqrt{2}\right)Ar\right) \\ & \left. - 48\xi^3\left(3(1+r)+A\left(-3+\left(5+4\sqrt{2}\right)r\right)\right)\right). \end{aligned} \tag{A30}$$

In practice, one can solve the ODEs as in the 2-D case.

References

Abarzhi, S.I. 1995 On the stability of steady-state solutions of the nonlinear Schrödinger equation. *J. Exp. Theore. Phys. (JETP)* **80** (1), 132–152.

Abarzhi, S.I. 1996*a* Group-theoretical analysis of the Rayleigh–Taylor instability. *J. Exp. Theor. Phys. (JETP)* **83** (5), 1012–1032.

Abarzhi, S.I. 1996*b* Group theory and nonlinear dynamics in Rayleigh–Taylor instability. *Phys. Scripta* **T66**, 238–242.

Abarzhi, S.I. 1998 Stabilization of nonlinear hydrodynamic instabilities by convection. *Phys. Rev. Lett.* **81** (2), 337–340.

Abarzhi, S.I. 1999 Stable steady flows in Rayleigh–Taylor instability. *Phys. Rev. E* **59**, 1729–1735.

Abarzhi, S.I. 2008 Review of nonlinear dynamics of the unstable fluid interface: conservation laws and group theory. *Phys. Scr.* **2008**(T132), 014012.

Abarzhi, S.I., Glimm, J. & Lin, A.-D. 2003 Dynamics of two-dimensional Rayleigh–Taylor bubbles for fluids with a finite density contrast. *Phys. Fluids* **15** (8), 2190–2197.

Abarzhi, S.I., Hill, D.L., Williams, K.C., Li, J.T., Remington, B.A., Martinez, D. & Arnett, W.D. 2023 Fluid dynamic mathematical aspects of supernova remnants. *Phys. Fluids* **35** (3), 034106.

Alon, U., Hecht, J., Ofer, D. & Shvarts, D. 1995 Power laws and similarity of Rayleigh–Taylor and Richtmyer–Meshkov mixing fronts at all density ratios. *Phys. Rev. Lett.* **74**, 534–537.

Banerjee, R., Mandal, L., Roy, S., Khan, M. & Gupta, M.R. 2011 Combined effect of viscosity and vorticity on single mode Rayleigh–Taylor instability bubble growth. *Phys. Plasmas* **18** (2), 022109.

Betti, R. & Hurricane, O.A. 2016 Inertial-confinement fusion with lasers. *Nat. Phys.* **12** (5), 435–448.

Betti, R. & Sanz, J. 2006 Bubble acceleration in the ablative Rayleigh–Taylor instability. *Phys. Rev. Lett.* **97**, 205002.

Bian, X., Aluie, H., Zhao, D.-X., Zhang, H.-S. & Livescu, D. 2020 Revisiting the late-time growth of single-mode Rayleigh–Taylor instability and the role of vorticity. *Physica D* **403**, 132250.

https://doi.org/10.1017/jfm.2025.10769 Published online by Cambridge University Press

BROUILLETTE, M. 2002 The Richtmyer–Meshkov instability. *Annu. Rev. Fluid Mech.* **34** (1), 445–445.
BURROWS, A. 2000 Supernova explosions in the universe. *Nature* **403** (6771), 727–733.
CABOT, W. & COOK, A. 2006 Reynolds number effects on Rayleigh–Taylor instability with possible implications for type Ia supernovae. *Nat. Phys.* **2**, 562–568.
CASEY, D.T. *et al.* 2017 Thermonuclear reactions probed at stellar-core conditions with laser-based inertial-confinement fusion. *Nat. Phys* vol. 13, pp. 1227–1231.
CHAN, W.H., JAIN, S.S., HWANG, H., NAVEH, A. & ABARZHI, S.I. 2023 Theory and simulations of linear and nonlinear two-dimensional Rayleigh–Taylor dynamics with variable acceleration. *Phys. Fluids* **35** (4), 042109.
CHANDRASEKHAR, S. 1961 *Hydrodynamic and Hydromagnetic Stability* Oxford Univ. Press.
CHANGWEN, L., ZUOLI, X. & YOUSHENG, Z. 2024 A review of research progresses on potential flow theory of single-mode fluid interfacial instabilities (in Chinese). *SCIENTIA SINICA Physica, Mechanica and Astronomica* **54** (10), 104702.
CLERY, D. 2015 Physics. Laser fusion, with a difference. *Science* **347** (6218), 111–112.
DIMONTE, G., RAMAPRABHU, P. & ANDREWS, M. 2007 Rayleigh–Taylor instability with complex acceleration history. *Phys. Rev. E* **76**, 046313.
DING, J.-C., T., S., YANG, J.-M., LU, X.-Y., ZHAI, Z.-G. & LUO, X.-S. 2017 Measurement of a Richtmyer–Meshkov instability at an air-SF_6 interface in a semiannular shock tube. *Phys. Rev. Lett.* **119**, 014501.
GLIMM, J., LI, XL & LIN, A.D. 2002 Nonuniform approach to terminal velocity for single mode Rayleigh–Taylor instability. *Acta Math. Appl. Sinica* **18**, 1–8.
GONCHAROV, V. 2002 Analytical model of nonlinear, single-mode, classical Rayleigh–Taylor instability at arbitrary Atwood numbers. *Phys. Rev. Lett.* **88** (13), 134502.
GOTTLIEB, S. & SHU, C.-W. 1998 Total variation diminishing Runge–Kutta schemes. *Math. Comput. Am. Math. Soc.* **67**, 73–85.
GUO, W.X. & ZHANG, Q. 2020 Universality and scaling laws among fingers at Rayleigh–Taylor and Richtmyer–Meshkov unstable interfaces in different dimensions. *Physica D* **403**, 132304.
HECHT, J., ALON, U. & SHVARTS, D. 1994 Potential flow models of Rayleigh–Taylor and Richtmyer–Meshkov bubble fronts. *Phys. Fluids* **6** (12), 4019–4030.
ISOBE, H., MIYAGOSHI, T., SHIBATA, K. & YOKOYAMA, T. 2005 Filamentary structure on the Sun from the magnetic Rayleigh–Taylor instability. *Nature* **434**, 478–481.
JACOBS, J.W. & SHEELEY, J.M. 1996 Experimental study of incompressible Richtmyer–Meshkov instability. *Phys. Fluids* **8** (2), 405–415.
JACOBS, J.W. & CATTON, I. 1988 Three-dimensional Rayleigh–Taylor instability Part 2. Experiment. *J. Fluid Mech.* **187**, 353–371.
JIANG, G.-S. & SHU, C.-W. 1996 Efficient implementation of weighted ENO schemes. *J. Comput. Phys.* **126** (1), 202–228.
KRECHETNIKOV, R. 2009 Rayleigh–Taylor and Richtmyer–Meshkov instabilities of flat and curved interfaces. *J. Fluid Mech.* **625**, 387–410.
KULL, H.J. 1983 Bubble motion in the nonlinear Rayleigh–Taylor instability. *Phys. Rev. Lett.* **51**, 1434–1437.
KULL, H.J. 1986 Nonlinear free-surface Rayleigh–Taylor instability. *Phys. Rev. A* **33** (3), 1957–1967.
LAYZER, D. 1955 On the instability of superposed fluids in a gravitational field. *Astrophys. J.* **122**, 1.
LHERM, V., DEGUEN, R., ALBOUSSIÈRE, T. & LANDEAU, M. 2022 Rayleigh–Taylor instability in impact cratering experiments. *J. Fluid Mech.* **937**, A20.
LI, X.-L., FU, Y.-W., YU, C.-P. & LI, L. 2021 Statistical characteristics of turbulent mixing in spherical and cylindrical converging Richtmyer–Meshkov instabilities. *J. Fluid Mech.* **928**, A10.
LIANG, Y., ZHAI, Z.-G., DING, J.-C. & LUO, X.-S. 2019 Richtmyer–Meshkov instability on a quasi-single-mode interface. *J. Fluid Mech.* **872**, 729–751.
LIU, C.-W., WU-WANG, H.-Z., ZHANG, Y.S. & XIAO, Z.-L. 2023*a* A decoupled mechanism of interface growth in single-mode hydrodynamic instabilities. *J. Fluid Mech.* **964**, A37.
LIU, C.-W., ZHANG, Y.S. & XIAO, Z.-L. 2023*b* A unified theoretical model for spatiotemporal development of Rayleigh–Taylor and Richtmyer–Meshkov fingers. *J. Fluid Mech.* **954**, A13.
LIU, L.-L., LIANG, Y., DING, J.-C., LIU, N.-A. & LUO, X.-S. 2018 An elaborate experiment on the single-mode Richtmyer–Meshkov instability. *J. Fluid Mech.* **853**, R2.
LUO, X.-S., WANG, X.-S. & SI, T. 2013 The Richtmyer–Meshkov instability of a three-dimensional interface with a minimum-surface feature. *J. Fluid Mech.* **722**, R2.
LUO, X.-S., ZHANG, F., DING, J.-C., SI, T., YANG, J.-M., ZHAI, Z.-G. & WEN, C.-Y. 2018 Long-term effect of Rayleigh–Taylor stabilization on converging Richtmyer–Meshkov instability. *J. Fluid Mech.* **849**, 231–244.

https://doi.org/10.1017/jfm.2025.10769 Published online by Cambridge University Press

MATSUO, K., SANO, T., NAGATOMO, H., SOMEKAWA, T., LAW, K.-F., MORITA, H., ARIKAWA, Y. & FUJIOKA, S. 2021 Enhancement of ablative Rayleigh–Taylor instability growth by thermal conduction suppression in a magnetic field. *Phys. Rev. Lett.* **127**, 165001.

MATSUOKA, C., NISHIHARA, K. & FUKUDA, Y. 2003 Erratum: nonlinear evolution of an interface in the Richtmyer–Meshkov instability. *Phys. Rev. E* **68**, 029902.

MIKAELIAN, K.O. 1998 Analytic approach to nonlinear Rayleigh–Taylor and Richtmyer–Meshkov instabilities. *Phys. Rev. Lett.* **80**, 508–511.

MIKAELIAN, K.O. 2003 Explicit expressions for the evolution of single-mode Rayleigh–Taylor and Richtmyer–Meshkov instabilities at arbitrary Atwood numbers. *Phys. Rev. E* **67**, 026319.

MIKAELIAN, K.O. 2008 Limitations and failures of the Layzer model for hydrodynamic instabilities. *Phys. Rev. E* **78**, 015303.

MIKAELIAN, K.O. 2009 Nonlinear hydrodynamic interface instabilities driven by time-dependent accelerations. *Phys. Rev. E* **79**, 065303.

MIKAELIAN, K.O. 2010 Analytic approach to nonlinear hydrodynamic instabilities driven by time-dependent accelerations. *Phys. Rev. E* **81**, 016325.

NI, W., ZENG, Q. & ZHANG, Y. 2023 Dependence of high-density-ratio Rayleigh–Taylor spike on initial perturbations. *Acta Mech. Sin.* **39** (3), 322181.

PIMENTEL-GARCIA, J.C. 2023 The full multi-wake vortex lattice method: a detached flow model based on potential flow theory. *Adv. Aerodyn.* **5**, 22.

RAMAPRABHU, P. & DIMONTE, G. 2005 Single-mode dynamics of the Rayleigh–Taylor instability at any density ratio. *Phys. Rev. E* **71**, 036314.

RAMAPRABHU, P., DIMONTE, G. & ANDREWS, M.J. 2005 A numerical study of the influence of initial perturbations on the turbulent Rayleigh–Taylor instability. *J. Fluid Mech.* **536**, 285–319.

RAMAPRABHU, P., DIMONTE, G., WOODWARD, P., FRYER, C., ROCKEFELLER, G., MUTHURAMAN, K., LIN, P.-H. & JAYARAJ, J. 2012 The late-time dynamics of the single-mode Rayleigh–Taylor instability. *Phys. Fluids* **24** (7), 074107.

RAMAPRABHU, P., KARKHANIS, V., BANERJEE, R., VARSHOCHI, H., KHAN, M. & LAWRIE, A.G.W. 2016 Evolution of the single-mode Rayleigh–Taylor instability under the influence of time-dependent accelerations. *Phys. Rev. E* **93**, 013118.

Rayleigh. 1883 Investigation of the character of the equilibrium of an incompressible heavy fluid of variable density. *Proc. Lond. Math. Soc* **s1–14** (1), 170–177.

RECKINGER, S.J., LIVESCU, D. & VASILYEV, O.V. 2011 Simulations of compressible Rayleigh–Taylor instability using the adaptive wavelet collocation method. *Bull. Am. Phys. Soc.* **64**.

RISTORCELLI, J.R. & CLARK, T.T. 2004 Rayleigh–Taylor turbulence: self-similar analysis and direct numerical simulations. *J. Fluid Mech.* **507**, 213–253.

ROE, P.L. 1981 Approximate Riemann solvers, parameter vectors, and difference schemes. *J. Comput. Phys.* **43** (2), 357–372.

SABET, N., HASSANZADEH, H., DE WIT, A. & ABEDI, J. 2021 Scalings of Rayleigh–Taylor instability at large viscosity contrasts in porous media. *Phys. Rev. Lett.* **126**, 094501.

SANDERS, R., MORANO, E. & DRUGUET, M.-C. 1998 Multidimensional dissipation for upwind schemes: stability and applications to gas dynamics. *J. Comput. Phys.* **145** (2), 511–537.

SHARP, D.H. 1984 An overview of Rayleigh–Taylor instability. *Physica D* **12-IN10** (1–3), IN1,11-IN1,11–10–10.

SOHN, S.-I. 2003 Simple potential-flow model of Rayleigh–Taylor and Richtmyer–Meshkov instabilities for all density ratios. *Phys. Rev. E* **67**, 026301.

SOHN, S.-I. 2004 Vortex model and simulations for Rayleigh–Taylor and Richtmyer–Meshkov instabilities. *Phys. Rev. E* **69**, 036703.

SOHN, S.-I. 2009 Effects of surface tension and viscosity on the growth rates of Rayleigh–Taylor and Richtmyer–Meshkov instabilities. *Phys. Rev. E* **80**, 055302.

SOHN, S.-I. 2011 Late-time vortex dynamics of Rayleigh–Taylor instability. *J. Phys. Soc. Japan* **80**, 084401.

TAYLOR, G.I. 1950 The instability of liquid surfaces when accelerated in a direction perpendicular to their planes. I. *Proc. R. Soc. Lond. A* **201** (1065), 192–196.

UCHIYAMA, Y., AHARONIAN, F.A., TANAKA, T., TAKAHASHI, T. & MAEDA, Y. 2007 Extremely fast acceleration of cosmic rays in a supernova remnant. *Nature* **449**, 576–578.

WEI, T. & LIVESCU, D. 2012 Late-time quadratic growth in single-mode Rayleigh–Taylor instability. *Phys. Rev. E* **86**, 046405.

WILLIAMS, K.C. & ABARZHI, S.I. 2021 Effect of dimensionality and symmetry on scale-dependent dynamics of Rayleigh–Taylor instability. *Fluid Dyn. Res.* **53** (3), 035507.

https://doi.org/10.1017/jfm.2025.10769 Published online by Cambridge University Press

WILLIAMS, K.C. & ABARZHI, S.I. 2022 Scale-dependent dynamics of Rayleigh–Taylor instability: group theory renormalization. *Frontiers in Applied Mathematics and Statistics* **7**, 735526.

Wolfram Research Inc. 2017 Mathematica, Version 11.2. Champaign, IL, 2017.

XIE, H., XIAO, M. & ZHANG, Y. 2024 A new idea for the unified rans predictions of turbulent mixing induced by interfacial instabilities (in Chinese). *Acta Aerodynamica Sinica* **42** (9), 1–13.

YAN, R., BETTI, R., SANZ, J., ALUIE, H., LIU, B. & FRANK, A. 2016 Three-dimensional single-mode nonlinear ablative Rayleigh–Taylor instability. *Phys. Plasmas* **23** (2), 022701.

YAN, Z., FU, Y.-W., WANG, L.-F., YU, C.-P. & LI, X.-L. 2022 Effect of chemical reaction on mixing transition and turbulent statistics of cylindrical Richtmyer–Meshkov instability. *J. Fluid Mech.* **941**, A55.

ZHANG, Q. 1998 Analytical solutions of Layzer-type approach to unstable interfacial fluid mixing. *Phys. Rev. Lett.* **81**, 3391–3394.

ZHANG, Q., DENG, S.Y. & GUO, W.X. 2018 Quantitative theory for the growth rate and amplitude of the compressible Richtmyer–Meshkov instability at all density ratios. *Phys. Rev. Lett.* **121**, 174502.

ZHANG, Q. & GUO, W.X. 2016 Universality of finger growth in two-dimensional Rayleigh–Taylor and Richtmyer–Meshkov instabilities with all density ratios. *J. Fluid Mech.* **786**, 47–61.

ZHANG, Q. & GUO, W.X. 2022 Quantitative theory for spikes and bubbles in the Richtmyer–Meshkov instability at arbitrary density ratios. *Phys. Rev. Fluids* **7**, 093904.

ZHANG, Y.-S., HE, Z.-W., XIE, H.-S., XIAO, M.-J. & TIAN, B.-L. 2020 Methodology for determining coefficients of turbulent mixing model. *J. Fluid Mech.* **905**, A26.

ZHANG, Q. & SOHN, S.-I. 1996 An analytical nonlinear theory of Richtmyer–Meshkov instability. *Phys. Lett. A* **212** (3), 149–155.

ZHANG, Q. & SOHN, S.-I. 1997 Padé approximation to an interfacial fluid mixing problem. *Appl. Maths Lett.* **10** (5), 121–127.

ZHANG, Y., LE, J. & TIAN, Y. 2024 Study on atomization characteristics of a kerosene jet in a supersonic crossflow. *Adv. Aerodyn.* **6**, 4.

ZHAO, Z.-Y., WANG, P., LIU, N.-S. & LU, X.-Y. 2020 Analytical model of nonlinear evolution of single-mode Rayleigh–Taylor instability in cylindrical geometry. *J. Fluid Mech.* **900**, A24.

ZHOU, Y. 2017*a* Rayleigh–Taylor and Richtmyer–Meshkov instability induced flow, turbulence, and mixing. I. *Phys. Rep.* **720–722**, 1–136.

ZHOU, Y. 2017*b* Rayleigh–Taylor and Richtmyer–Meshkov instability induced flow, turbulence, and mixing. II. *Phys. Rep.* **723–725**, 1–160.

ZHOU, Y. 2024 *Hydrodynamic Instabilities and Turbulence: Rayleigh–Taylor, Richtmyer–Meshkov, and Kelvin–Helmholtz Mixing*. Cambridge University Press.

ZHOU, Y., CLARK, T.T., CLARK, D.S., GAIL GLENDINNING, S., AARON SKINNER, M., HUNTINGTON, C.M., HURRICANE, O.A., DIMITS, A.M. & REMINGTON, B.A. 2019 Turbulent mixing and transition criteria of flows induced by hydrodynamic instabilities. *Phys. Plasmas* **26** (8), 080901.

ZHOU, Y., SADLER, J. & HURRICANE, O. 2024 Instabilities and mixing in inertial confinement fusion. *Annu. Rev. Fluid Mech.* **57**, 197–225.

ZHOU, Y. *et al.* 2021 Rayleigh–Taylor and Richtmyer–Meshkov instabilities: A journey through scales. *Physica D* **423**, 132838.

ZUFIRIA, J.A. 1988 Bubble competition in Rayleigh–Taylor instability. *Phys. Fluids* **31** (3), 440–446.

https://doi.org/10.1017/jfm.2025.10769 Published online by Cambridge University Press